



**Politecnico
di Torino**

Master's Degree Thesis

Master's Degree course in INGEGNERIA
MECCANICA (MECHANICAL ENGINEERING)

**Thermal transport in nanostructured
thin films: the challenge of a
microscopic understanding**

Supervisor

Prof. Matteo Fasano

External supervisors

Doct. Valentina Giordano

Doct. Paolo Maioli

Candidate

Giulio Catalucci

A.A. 2021/2022

Abstract

One of the main challenges for our modern society consists in reducing the heat losses associated with energy consumption: indeed, about two thirds of produced energy is lost as heat, whatever the energy source and processing. Optimizing materials and processes for reducing heat dissipation, increasing thermal insulation, and converting heat into other forms of energy is at the focus of an intense research effort. In this context, nanostructuration has arisen as a most promising approach: the presence of interfaces and the intertwining of different materials at the nanoscale has shown to effectively act on the quasi-particle responsible for heat transport – phonons – and not on other functional properties. In this work, I will study the properties of phonons (energy and lifetime) in Germanium Telluride, a semiconducting material interesting for many applications, whose thermal properties can be greatly transformed through nanostructuration. To conclude, the thesis includes measurements obtained with Pump and Probe spectroscopy with testing developed at the Institut Lumimère Matière of Lyon.

Contents

1	Introduction	1
1.1	Nanostructured materials: a promising approach	2
2	Phonon heat transport	4
2.1	Thermal transport in semiconductors	4
2.2	Basis of phonon theory	4
2.3	Phonon scattering	6
2.4	Nanostructuring	8
2.5	Modification of thermal conductivity	11
3	Material overview	13
3.1	The investigated material: GeTe	13
3.1.1	Amorphous phase	15
3.1.2	Crystalline phase	16
3.2	Metavalent bonding	17
3.3	GeTe applications	19
3.3.1	Thermoelectric applications	19
3.3.2	Phase change memories applications	20
3.4	Sample production	22
3.5	State of the art of thermal and phonon measurements on GeTe thin film	24
4	High frequency phonons detection methods	25
4.1	Detection strategy	25
4.2	Pulse echo method	27
4.3	Phonon-resonance spectroscopy	30

4.4	Brillouin-oscillation method	31
4.5	Comparison between different methods	33
5	Ultrafast acoustic pump-probe experiments	36
5.1	Samples	38
5.2	Experimental set-up	41
5.2.1	Set-up n°1	42
5.2.2	Set-up n°2	47
5.2.3	Lock-in acquisition	47
6	Results	50
6.1	Samples with transducer	51
6.2	Samples without transducer	54
6.3	Attenuation analysis	64
7	Conclusions	67
A	Longitudinal vibrations of the sample	68
A.1	Slab model	68

List of Figures

1.1	Wasted energy	1
2.1	Phonon scattering mechanisms	7
2.2	Number of publications in each year	9
2.3	Nanomaterials types	10
3.1	Periodic table of elements	13
3.2	Phase change material operations	15
3.3	Bonds of amorphous structure	16
3.4	Atomic image of R3m structure	17
3.5	Quantum-mechanical map	18
3.6	Comparison between different kinds of memories	20
3.7	Thermal-induced lattice transformation	21
3.8	A schematic of sputter deposition	23
4.1	Attenuation as a function of sample thickness	26
4.2	Scheme of pulse echo method	27
4.3	Sample geometry with transducer	29
4.4	Sample structure without transducer	30
4.5	Scheme of phonon-resonance spectroscopy	31
4.6	Scheme of Brillouin-oscillation method	32
4.7	Fourier series of order 1	34
4.8	Fourier series of order 3 and 80	35
5.1	Basic principle of Pump and Probe	36
5.2	Experimental signal of a Ultrafast response of an Au nanoparticle	38

5.3	Picture of GeTe sample with Gold transducer used for measurements	39
5.4	Different types of samples	40
5.5	Optical index and absorption coefficient of GeTe	41
5.6	Experimental set-up	42
5.7	Coherent Verdi V10 laser source	42
5.8	Delay line	43
5.9	Photodiode	44
5.10	Photodiode	44
5.11	Mechanical Chopper	45
5.12	Long-time configuration	46
5.13	Short-time configuration	46
5.14	Lock-in amplifier	48
6.1	Relative optical reflectivity variation of a GeTe sample (200 nm) with a Gold transducer (15 nm) and Silica substrate	51
6.2	Relative optical reflectivity variation of a GeTe sample (200 nm) with an Aluminum transducer (20 nm) and Silica substrate	52
6.3	Relative optical reflectivity variation of a GeTe sample (400 nm) with a Gold transducer (40 nm) and Silicon substrate	53
6.4	Fit of the relative optical reflectivity variation of a GeTe sample (400 nm) with Gold transducer (40 nm) and Silicon substrate.	54
6.5	Relative optical reflectivity variation of a GeTe sample (100 nm) without transducer and Silica substrate	55
6.6	Relative optical reflectivity variation of a GeTe sample (400 nm) without transducer and Silica substrate	56
6.7	Fit of the relative optical reflectivity variation without the exponential component of a GeTe sample (100 nm) without transducer and Silica substrate.	57
6.8	Fit of the relative optical reflectivity variation without the exponential component of a GeTe sample (400 nm) without transducer and Silica substrate	58

6.9	Plot of harmonics coefficient (absolute value $\times 10^{-6}$) of a GeTe sample (100 nm) without transducer and Silica substrate. . . .	59
6.10	Plot of harmonics coefficient (absolute value $\times 10^{-6}$) of a GeTe sample (400 nm) without transducer and Silica substrate. . . .	60
6.11	Approximation of the excitation profile in a 400 nm layer . . .	62
6.12	Excitation profile in a 400 nm layer	63
6.13	Plot of attenuation values	65
A.1	Single slab	69
A.2	Normalized displacement field of symmetric modes	70
A.3	Normalized displacement field of anti-symmetric modes	71

List of Tables

4.1	A brief comparison of the detection methods introduced	33
5.1	List of all the samples measured	40

Chapter 1

Introduction

The reduction of energy consumption is one of the major objectives due to the global warming and increasing cost related to the conventional fossil fuel sources. It is possible to intervene through renewable sources but also by increasing the efficiency of exploitation of primary energies. In fact, as can be seen in Fig. 1.1, about two third of produced energy is lost as heat and it is necessary to proficiently convert heat into a usable form of energy.

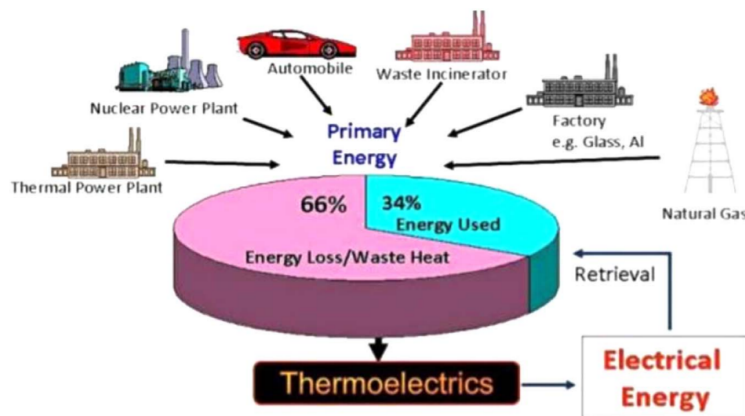


Figure 1.1: Diagram showing wasted energy. Figure taken from ref. [1] (©Elsevier 2017).

For example, the engine in a car uses only about 30 % of the gasoline it burns to move the car. The rest is dissipated as heat [2]. To solve this problem, several studies have been done on materials that allow the reduction of heat

dissipation by increasing thermal insulation and exploiting the heat for other forms of energy.

1.1 Nanostructured materials: a promising approach

An interesting approach for this context is nanostructuring. Nanostructured materials are important because they allow the combination of low thermal conductivity with good electrical properties, unlike traditional single materials. Despite a multitude of studies on nanostructured materials (nanocrystalline, superlattices, nanocomposites...), a whole understanding of their thermal transport is still missing, therefore the optimization for heat management is still very limited. The aim of this thesis is to study the effect of nanostructuring on thermal transport in GeTe (Germanium Telluride), a semiconducting material of interest for many applications. One of the most important is thermoelectricity: the combination of low thermal conductivity and good electrical properties of the nanocomposites allows the exploitation of thermoelectric effects to transform, through the Seebeck effect, the wasted heat into energy. The improvement of the thermoelectric properties through nanostructuring would allow a reduction of wasted heat. Another very important application is that of phase change random access memories (PCRAM): a phase change material is able to switch very rapidly between two phases (e.g. amorphous and crystalline) with extremely different electronic properties. The fact that GeTe is a phase-change material allows the material to be a good candidate for efficient coding of the information in the phase state. In this case, as I will detail later the study of GeTe and the improvement of its properties through nanostructuring would allow increasing the coding efficiency by decreasing the energy required for data storage. All these properties of nanocomposites are due to the presence of interfaces that act in the inhibition of phonons, which are responsible for heat transport in semiconductors. In this thesis, I will study the properties of phonons (energy and lifetime) using a technique that allows us to measure phonons with wavelengths of tens of nanometers in thin films: ultrafast

acoustic pump-probe technique. This experimental campaign is developed in the FemtoNanoOptics group at Institut Lumière Matière of Université de Lyon.

Chapter 2

Phonon heat transport

2.1 Thermal transport in semiconductors

For understanding the background of this work it is necessary to introduce the properties of semiconductors. Semiconductors are materials, belonging to the category of semimetals, which can assume a resistivity higher than that of conductors (generally metals) and lower than that of insulators (such as most ceramic). They are the basis of main solid-state electronic and microelectronic devices such as transistors and diodes. The properties of such materials become interesting if they are doped with impurities. Their characteristics such as resistance, mobility and concentration of charge carriers are important to determine the field of use. It is therefore important to understand how to vary the characteristics of the semiconductor to obtain the desired thermal and electrical properties. The latter vary according to the material considered: there are two types of heat carriers, phonons and electrons. In insulators and semiconductors phonons heat transport dominates because there are relatively few free electrons [3].

2.2 Basis of phonon theory

Heat conduction can be considered as a measure of the energy of the vibrations of the atoms in the material. The energy of each vibration is quantized: a phonon is a quantum of vibrational energy. A phonon is thus the quantum

mechanical description of an elementary vibrational motion in which a lattice of atoms or molecules uniformly oscillates at a single frequency. The energy of the material, related to temperature, is the sum of the energy of all populated phonon states. In other words, the total energy of the material is given by the sum of the energies $\hbar\omega$ of all phonons, weighed by their temperature dependent population (Bose-Einstein distribution) and their density of states (how many phonons with a given energy).

A phonon is the quantum mechanical conversion of normal modal vibration in classical mechanics. A main property of phonons is their wave-particle duality: normal modes have particle-like behaviour under quantum mechanics but wave-like phenomena in classical mechanics.

The energy of phonon states are:

$$\epsilon = \left(n + \frac{1}{2} \right) \hbar\omega \quad (2.1)$$

where ω is the angular frequency, n its quantum number and \hbar is the plank constant. The levels are equally spaced:

$$\frac{1}{2}\hbar\omega, \frac{3}{2}\hbar\omega, \frac{5}{2}\hbar\omega\dots \quad (2.2)$$

where the term $\frac{1}{2}\hbar\omega$ is the zero point energy of the mode. To push the lattice to the next energy level, an exact amount of energy $\hbar\omega$ must be supplied [4]. If a solid has more than one type of atom in the unit cell, there are two types of phonons: “acoustic” and “optical” phonons. Acoustic phonons have the sound speed when the wavevector is small and have zero frequency when the wavevector is null, while optical phonons always have a finite frequency, even for a null or very small wavevector.

At zero temperature, a crystal lattice is in its ground state, and contains no phonons (no vibrational energy). When the lattice is heated at a non-zero temperature, its energy fluctuates randomly around some mean value. This energy fluctuation is caused by random lattice vibrations and can be described using the concept of a gas of phonons. Since the phonons are generated by the temperature of the lattice, they are sometimes called thermal phonons.

A phonon of wavevector k will interact with particles like photons, neutrons

and electrons as if it had a momentum $\hbar k$. Since the vibration is not associated with mass transfer, the phonon "momentum" is not a true physical momentum (the net mechanical momentum of a phonon is indeed zero), and is called a "quasimomentum". The latter is conserved in any phonon scattering process. Considering a three-phonon scattering process, the energy conservation is represented by:

$$\hbar\omega_1 + \hbar\omega_2 - \hbar\omega_3 = 0 \quad (2.3)$$

The momentum conservation is instead expressed through the corresponding phonon wavevectors as:

$$k_1 + k_2 - k_3 = 0 \quad (2.4)$$

In Eq. 2.4 a nonzero reciprocal lattice vector G can be added [4]:

$$k_1 + k_2 - k_3 = G \quad (2.5)$$

2.3 Phonon scattering

As already mentioned, at room temperature, the atomic lattice of materials is not static, and atoms actually vibrate around their mean positions. The vibrations of the lattice increase with the increase in temperature and this increased movement leads the phonons to interact. In the phonon gas description, the phonon is seen as a quasiparticle moving with a given velocity and carrying a given energy. It can then interact with other (quasi)particles, which can be seen as a collision, affecting the direction of the phonon, which is scattered, and possibly its velocity.

Phonons have several scattering mechanisms (Fig. 2.1): Umklapp phonon-phonon scattering, phonon-electron scattering, phonon-impurity scattering and phonon-boundary scattering [5]. Every scattering mechanism is represented by a relaxation ratio $\frac{1}{\tau}$, the inverse of the relaxation time τ , which represents the typical time between two scattering events.

The overall relaxation time can be thought of as a lifetime: the average time delay between two scattering events of whatever kind. As such, it allows to define the mean free path, the distance travelled by the phonon before being scattered, which is $l = v\tau$, with v the group velocity. This distance is the

distance over which a phonon can carry its energy, thus heat. Scattering mechanisms, affecting phonon mean free path, can thus affect thermal transport.

The overall relaxation rate can be computed through the Mattiessen's rule as:

$$\frac{1}{\tau_c} = \frac{1}{\tau_U} + \frac{1}{\tau_{ph-e}} + \frac{1}{\tau_M} + \frac{1}{\tau_B} \quad (2.6)$$

where τ_U is due to Umklapp scattering, τ_{ph-e} to phonon-electron scattering, τ_M to mass-difference impurity scattering and τ_B to phonon-boundary scattering.

This rule is not valid if the scattering mechanisms depend on each other, as individual scattering rates can be summed only if they are independent from each other [6].

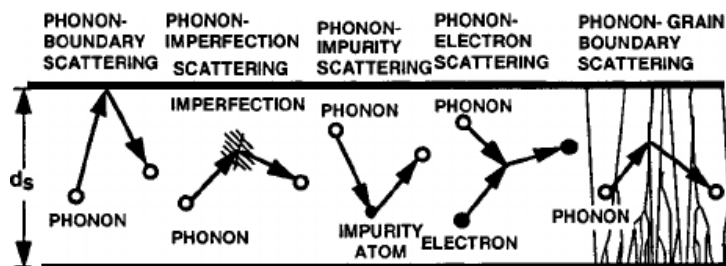


Figure 2.1: Phonon scattering mechanisms that reduce the thermal conductivity. Figure taken from ref. [7]

- **Umklapp scattering**

Umklapp scattering is an anharmonic phonon-phonon coupling. It is temperature driven as phonon population increases with temperature. As such, its characteristic relaxation time is temperature dependent, and the process becomes more important at high temperature. In our case it can be considered negligible, due to the dominant role of defect scattering.

- **Phonon-electron scattering**

In the early years, the phonon-electron scattering was not considered in the computation of lattice thermal conductivity. Instead the phonon

electron scattering can have in some case a strong impact in 2D metallic materials due to the high density of electron states [8]. However for semiconductors it can be assumed that contribution to thermal conductivity by phonon-electron scattering is negligible [9].

- **Mass-difference impurity scattering**

The presence of impurities in a material generates scattering which leads to a reduction in thermal conductivity. The greater the mass, the volume and the stiffness difference between the host atom and the impurity (isotope) atom, the greater the scattering, For example, the naturally developed isotopes in Si create phonon scattering events which can lower the thermal conductivity from that of isotopically pure Si by 14% at room temperature. This kind of mass-difference impurity scattering process can be used to reduce the thermal conductivity in alloys [10].

- **Phonon-boundary scattering**

Phonon-boundary scattering is a scattering process between phonons and the different interfaces of the material. If the characteristic length (for example film thickness) is comparable to the mean free path of the phonon, the boundary scattering becomes very important and the thermal conductivity is even dominated by the scattering with the interface of the thin film. Subsequently, the thermal conductivity becomes size dependent [11]. Boundary scattering reduces the phonon mean free path (and thus the thermal conductivity) and this is why boundary scattering is particularly important for low-dimensional nanostructures [12].

For the purpose of our project we plan to increase phonon-boundary scattering to reduce thermal conductivity through nanostructuring.

2.4 Nanostructuring

Nanomaterials are defined as materials having at least one dimension smaller than 100 nm and are having rapid development due to their potential ap-

plications in many fields: nanoelectronics, magnetic, structural components, biosensors, biomaterials. Contrary to bulk materials, nanomaterials have thermal properties which depend on boundary effects due to the small size. Materials reduced to nanoscale may suddenly exhibit different properties than those they exhibit on a macroscopic scale, making unique applications possible. For this reason, the number of studies and articles on nanostructured materials has grown in recent years as highlighted by Fig. 2.2 which shows the increasing number of publications on nanoscale, phonon and thermoelectrics.

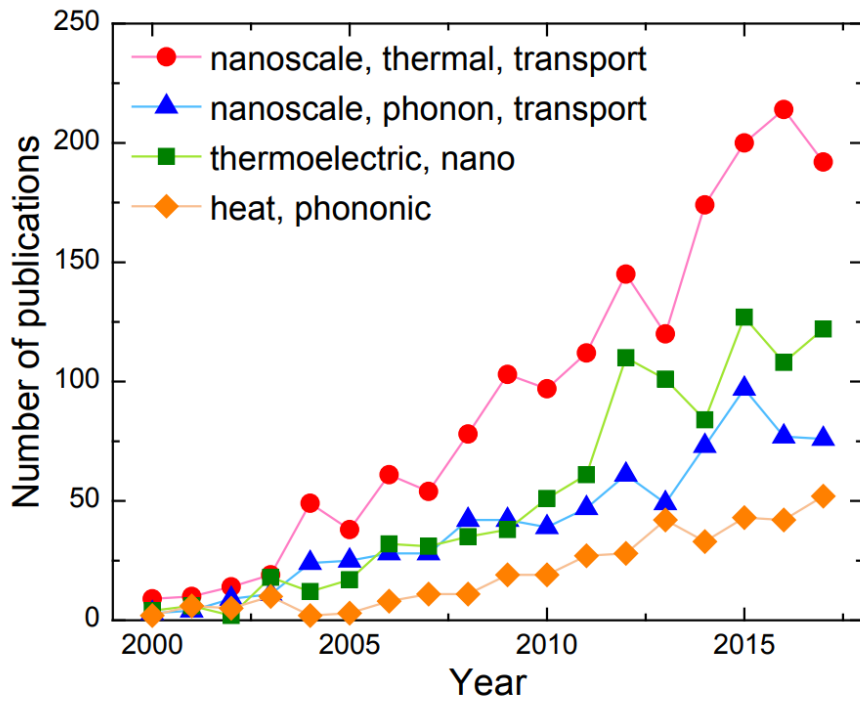


Figure 2.2: Number of publications related to nanostructured materials, phonon, thermal transport and thermoelectrics in each year. Figure taken from ref. [13].

Four types of nanomaterials can be considered (Fig. 2.3):

- **Zero-dimensional**

Zero-dimensional nanomaterials (0D) are materials with three nanometric dimensions, such as a sphere with a diameter of 1-50 nm.

- **One-dimensional**

One-dimensional nanomaterials (1D) are materials having one dimension of 1-100nm and the other two dimensions in the macroscale, like nanotubes, nanofibers and nanowires.

- **Two-dimensional**

Two-dimensional nanomaterials (2D) are materials with two dimensions in nanoscale and one dimension in the macroscale, like thin films, nanosheets and nanowalls.

- **Three-dimensional**

Three-dimensional nanomaterials are materials with no nanometric dimension and all dimensions in macroscale. For example bulk materials are 3D nanomaterials composed of individual blocks with nanometer scale.

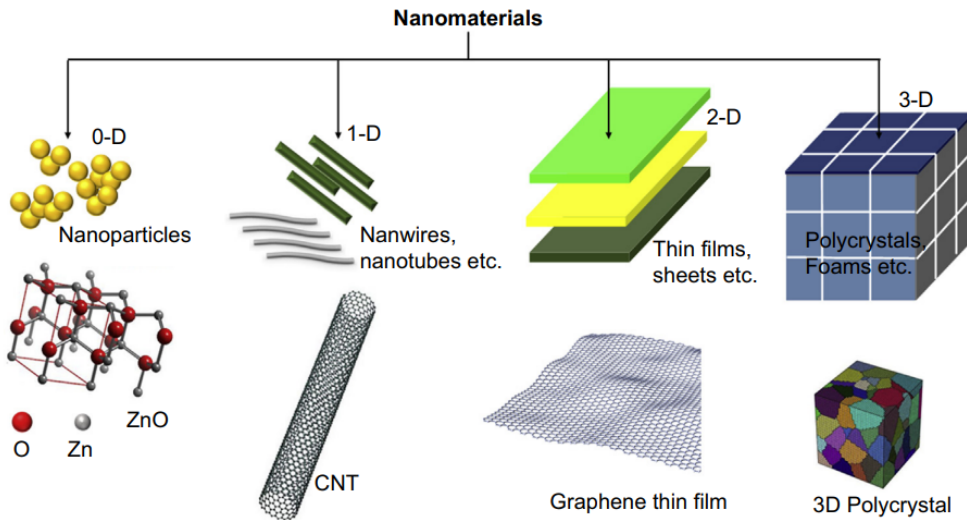


Figure 2.3: Representation of zero-dimensional, one-dimensional, two-dimensional and three-dimensional nanomaterials. Figure taken from ref. [14]

As already mentioned, the modification of the phonon behavior can be carried out through the nanostructuring of the material.

We now focus on thermal transport to understand how nanostructuring can be modified and improved.

2.5 Modification of thermal conductivity

As already mentioned, the thermal transport in semiconductors is assured by phonons. In fact, the thermal conductivity depends on phonon wavelength and on temperature. The dependence on phonon wavelength can be shown through the Boltzmann transport approach and single relaxation time approximation:

$$k_T = \frac{1}{3} \int c_v(\omega) v(\omega) l(\omega) g(\omega) d\omega \quad (2.7)$$

with $c_v(\omega)$ the phonon specific heat (which depends on the phonon population), $v(\omega)$ its velocity, $l(\omega)$ its mean free path and $g(\omega)$ the phonon density of states.

It is important to notice that phonons participate to heat transport with a relative weight which depends on their energy and on the actual temperature. Indeed, the energy distribution over all phonons at a given temperature has the profile of a bell centered at the wavelength λ_{dom} :

$$\lambda_{dom} = \frac{h v_s}{2.82 k_B T} \quad (2.8)$$

with v_s the sound velocity in the material, T the temperature, h the Plank constant and k_B the Boltzmann constant. The result gives the wavelength of phonons dominating heat transport at a given temperature.

If we assume that only phonons at the dominant phonon wavelength participate to heat transport and we assume that all phonons have the same velocity i.e. the sound velocity v and the same mean free path, the thermal conductivity can be simplified as

$$k_T = \frac{1}{3} c_v v l \quad (2.9)$$

From Eq. 2.8, it is clear that at low temperature, only long wavelength (μm to mm) low energy phonons will be active for heat transport, while at room temperature the most efficient carriers will be phonons with wavelengths in the nanometric and sub-nanometric range, which have frequencies in the THz range. Therefore, depending on the temperature at which we plan to manipulate the thermal transport, it is possible to use nanostructured materials at different lengthscales in order to act on the phonon with dominant

wavelength. To sum up, the effect of nanostructuration will depend on how many phonons are effectively perturbed and on the weight of their contribution to the total thermal conductivity. In order to understand the specific microscopic mechanisms a different approach is required: instead of measuring the thermal conductivity through the integral (Eq. 2.7) we focus on the propagation of the single phonons. This is the strategy of my thesis: understand how nanostructuration affects phonon propagation and thus thermal transport, in order to control it.

Chapter 3

Material overview

3.1 The investigated material: GeTe

Germanium telluride (GeTe) is a chalcogenide material: this means that it is composed of one of the elements of the chalcogen family present in the periodic table of the elements (Fig. 3.1). In the case of GeTe, this is the Tellurium. The semiconductor properties of chalcogenide-based materials were discovered in the 1950s by Kolomiets and Goryunova at the Ioffe Physical-Technical Institute. In 1968, however, Ovshinsky was the first to observe a change in the structure of these materials by studying the STAG materials ($Si_{12}Te_{48}As_{30}Ge_{10}$) that were already used for commercial purposes in the 1970s [15].

The figure shows a standard periodic table of elements. The elements are arranged in rows and columns. The element Tellurium (Te), with atomic number 52, is highlighted with a red square. The periodic table includes elements from Hydrogen (1) to Oganesson (118). The chalcogen group (Group 16) is highlighted in green, and the halogen group (Group 17) is highlighted in yellow. The noble gases (Group 18) are highlighted in light blue. The lanthanide and actinide series are shown below the main table, with asterisks indicating their positions.

1 H																	2 He
3 Li	4 Be											5 B	6 C	7 N	8 O	9 F	10 Ne
11 Na	12 Mg											13 Al	14 Si	15 P	16 S	17 Cl	18 Ar
19 K	20 Ca	21 Sc	22 Ti	23 V	24 Cr	25 Mn	26 Fe	27 Co	28 Ni	29 Cu	30 Zn	31 Ga	32 Ge	33 As	34 Se	35 Br	36 Kr
37 Rb	38 Sr	39 Y	40 Zr	41 Nb	42 Mo	43 Tc	44 Ru	45 Rh	46 Pd	47 Ag	48 Cd	49 In	50 Sn	51 Sb	52 Te	53 I	54 Xe
55 Cs	56 Ba	* 71 Lu	* 72 Hf	* 73 Ta	* 74 W	* 75 Re	* 76 Os	* 77 Ir	* 78 Pt	* 79 Au	* 80 Hg	* 81 Tl	* 82 Pb	* 83 Bi	* 84 Po	* 85 At	* 86 Rn
87 Fr	88 Ra	* 103 Lr	* 104 Rf	* 105 Db	* 106 Sg	* 107 Bh	* 108 Hs	* 109 Mt	* 110 Ds	* 111 Rg	* 112 Cn	* 113 Nh	* 114 Fl	* 115 Mc	* 116 Lv	* 117 Ts	* 118 Og
		* 57 La	* 58 Ce	* 59 Pr	* 60 Nd	* 61 Pm	* 62 Sm	* 63 Eu	* 64 Gd	* 65 Tb	* 66 Dy	* 67 Ho	* 68 Er	* 69 Tm	* 70 Yb		
		* 89 Ac	* 90 Th	* 91 Pa	* 92 U	* 93 Np	* 94 Pu	* 95 Am	* 96 Cm	* 97 Bk	* 98 Cf	* 99 Es	* 100 Fm	* 101 Md	* 102 No		

Figure 3.1: Periodic table of elements. The red square corresponds to chalcogen

Crystalline GeTe is a semiconductor intrinsically p-doped due to a high number of germanium vacancies (10^{21} carriers/ cm^3). Being a semiconductor, thermal transport is mainly carried out by phonons.

Moreover GeTe is a phase change material which is subjected to reversible transition between amorphous and crystalline phase when heated. In electronic devices the switch between the phases is realized heating the material by an electrical or optical pulse, which allows for a very fast phase change. If we bring the material initially in its amorphous phase to high temperature (but lower than the melting temperature) it will rapidly crystallize. This process is called SET. To return to the amorphous structure, it is instead necessary to go beyond the melting temperature and rapidly cool down in order to freeze the atomic structure in a disordered state. This process is called RESET (Fig. 3.2).

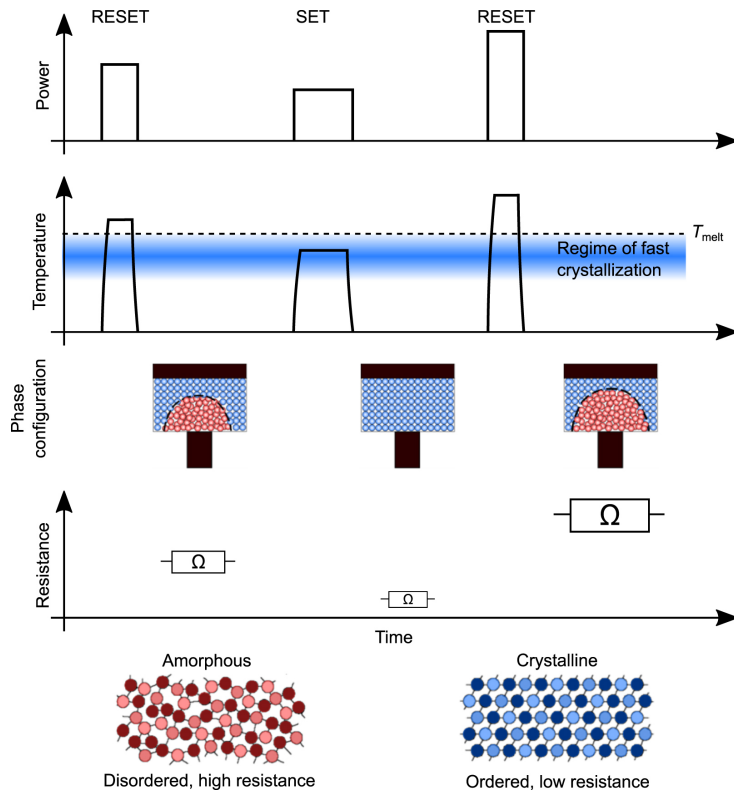


Figure 3.2: Operation of SET and RESET on a phase change material in order to pass from amorphous to crystalline phase and vice versa. The typical device has a mushroom shape, leading to a maximum heating in the bottom position, as shown in the sketch. Figure taken from ref. [16].

3.1.1 Amorphous phase

The change of phase induces a strong change of optical and electrical properties. In fact the amorphous phase has a low optical reflectivity and a high resistivity [16]. The disordered structure of the amorphous is mainly composed by the three types of bonds shown in Fig. 3.3.

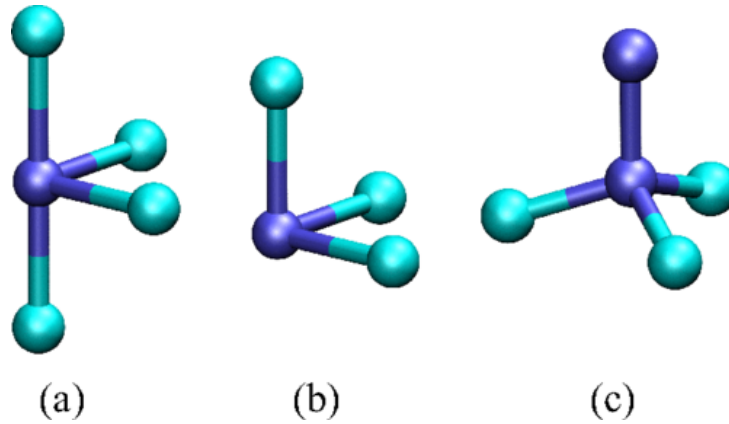


Figure 3.3: GeTe atoms environments (GeTe) are shown with Ge atoms in blue and Te atoms in cyan: (a) defective octahedra, (b) pyramids, and (c) tetrahedra with a wrong Ge-Ge bond. Figure from [17] (©American Physical Society 2015).

3.1.2 Crystalline phase

The transformation of GeTe from the amorphous phase to the crystalline phase induces a significant change in its resistance and optical properties [18]. Indeed the crystalline phase has a low resistivity and a high optical reflectivity. At atmospheric ambient conditions, crystalline GeTe has a typical rhombohedral structure $R\bar{3}m$, as shown in Fig. 3.4.

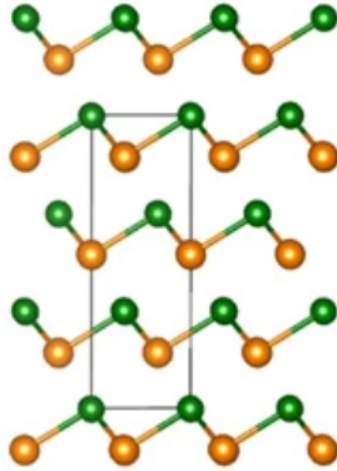


Figure 3.4: Atomic image of R3m structure. Figure taken from ref. [18].

Another difference between the amorphous state and the crystalline state is the presence of particular bonds called "metavalent" bonds which are the cause of the difference in properties. It has been recently proposed as a new kind of bond and is located between the metallic and the covalent bond and with a portfolio of properties that differs significantly from both. This type of bond is present only in the crystalline structure.

3.2 Metavalent bonding

One of the main characteristics of GeTe is the large contrast of both electrical and optical properties between the amorphous and crystalline phases, which is due to metavalent bonds. Fig. 3.5 shows a map which allow to distinguish metallic, covalent and ionic materials. The axes of this map correspond to two basic phenomena: the transfer of electrons between two atoms, leading to ionic behaviour and the sharing of electrons between them describing the covalent bond. These two coordinates separate different types of chemical bonding in solids. Materials with metavalent bonding stand in a defined area and this explains the singular characteristics [19]. In fact, it has been

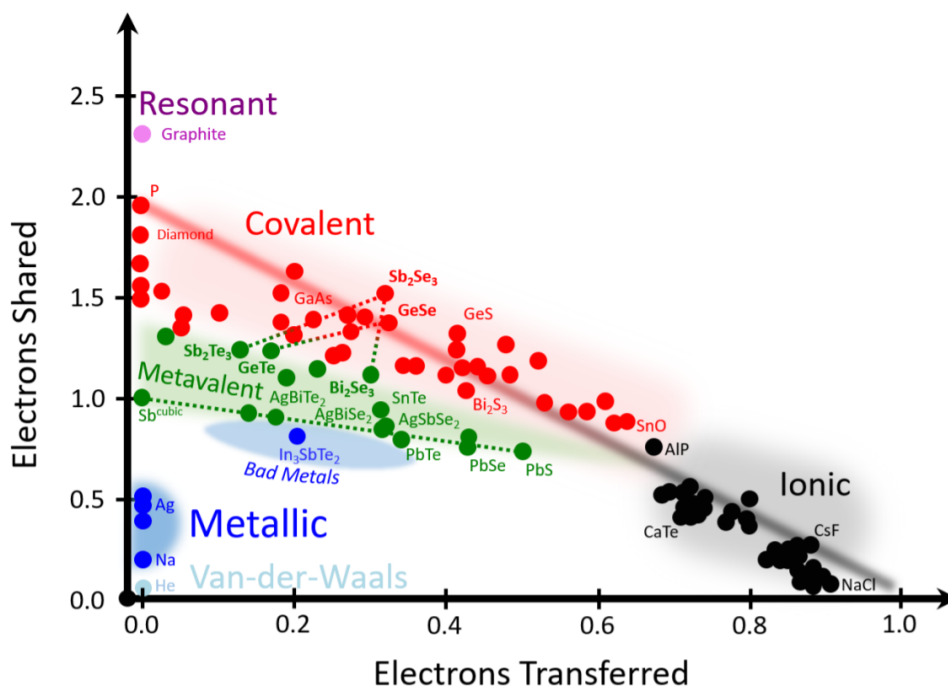


Figure 3.5: A quantum-mechanical map for materials, spanned by bonding descriptors in a two-dimensional plane. Figure taken from [19].

demonstrated that metavalently bonded solids are characterized by a unique combination of properties, including anharmonicity, moderate electrical conductivities, effective coordination numbers incompatible with the traditional “8-N” view of covalent bonding, a large chemical bond polarizability, leading to high values of the Born effective charge as well as a large optical dielectric constant [20]. This metavalent bonding seems at the origin of the physical properties which make GeTe promising for two important applications: for thermoelectric applications and for phase change random access memories (PCRAM).

3.3 GeTe applications

3.3.1 Thermoelectric applications

Thermoelectric materials are materials which can convert heat energy into electrical energy or vice versa. The efficiency of the thermoelectric conversion is measured through the quality factor

$$ZT = \frac{S^2 \sigma T}{k_T} \quad (3.1)$$

where S is the Seebeck coefficient, given by the ratio between the induced voltage and the applied temperature gradient, σ is the electric conductivity, T the temperature in Kelvin and k_T the thermal conductivity. Due to the metavalent bonding, GeTe owns a series of electronic properties (ex.: high valley degeneracy, band anisotropy...) which tend to increase the Seebeck coefficient S . For this reason, GeTe is considered an extremely promising thermoelectric material for mid-temperature applications (300-600K). Apparently, GeTe was not of further interest due to its high p-type carrier concentration of $\approx 8.7 \times 10^{20} \text{ cm}^{-3}$ because of the intrinsic Ge vacancies, which gives rise to a high σ of $\approx 8000 \text{ Scm}^{-1}$, high electrical thermal conductivity and a low S of $\approx 34 \text{ VK}^{-1}$ at room temperature. What makes GeTe a promising thermoelectric material is that its ZT can be strongly enhanced through reduction of the lattice thermal conductivity k_T through different methods: by hierarchical phonon scattering with nanostructures, by lattice/bonding anharmonicity, by adding of rattling modes, and superionic

substructures with liquid like cation disordering [21]. Since nanostructuration represents a promising strategy (because it is not supposed to affect the electronic properties while further reducing the thermal conductivity), in this project we are going to study its effect on GeTe thermoelectric properties.

3.3.2 Phase change memories applications

The metavalent bonding is considered responsible also for the phase change characteristics of GeTe, which make it suitable for Phase Change Memories applications. As already mentioned, these two phases have dramatically different electrical properties, being the amorphous insulating and the crystal semiconductive. For this characteristics, GeTe can be used for Phase change memories applications . Phase-change memory is a type of non-volatile random-access memory (PCRAM). As shown in Fig. 3.6, this kind of memories fills the gap that exists between non-volatile and volatile memories, allowing us to have fast access to data at lower cost.

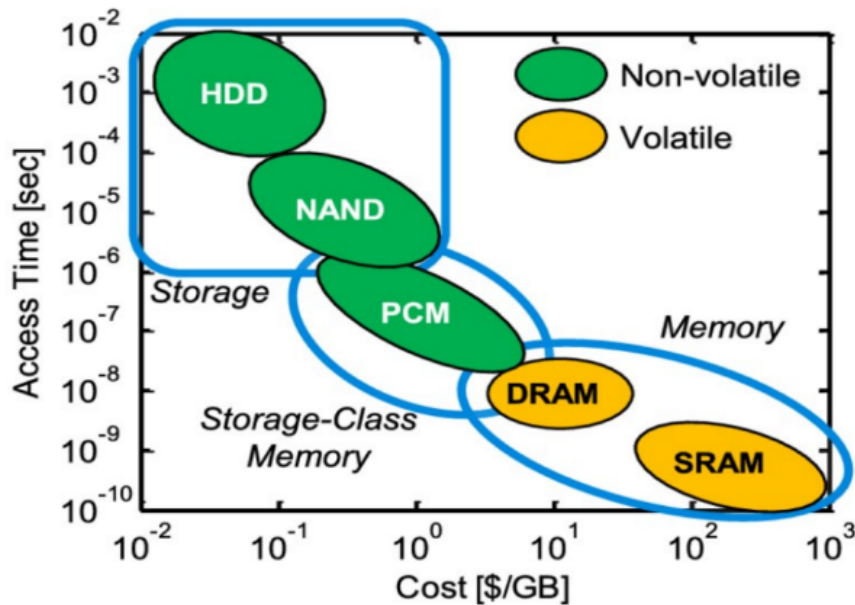


Figure 3.6: Comparison between different kinds of memories. Figure taken from [22]

These devices exploit the differences in electric properties between the amor-

phous phase and crystalline phase for coding the information. For example, for an amorphous phase, there will be a larger electric resistivity (coded as bit 0) with respect to the crystalline phase (bit 1).

A voltage is applied to the phase change material that will heat-up to a critical temperature by Joule effect. As already mentioned, to induce the crystalline GeTe it is essential to heat the amorphous GeTe above the glass transition temperature, followed by a slow quenching process. The amorphous GeTe can be achieved by heating its crystalline state above melting temperature that is subsequently subjected to a rapid cooling. Such repetitive transition processes are schematically illustrated in Fig. 3.7.

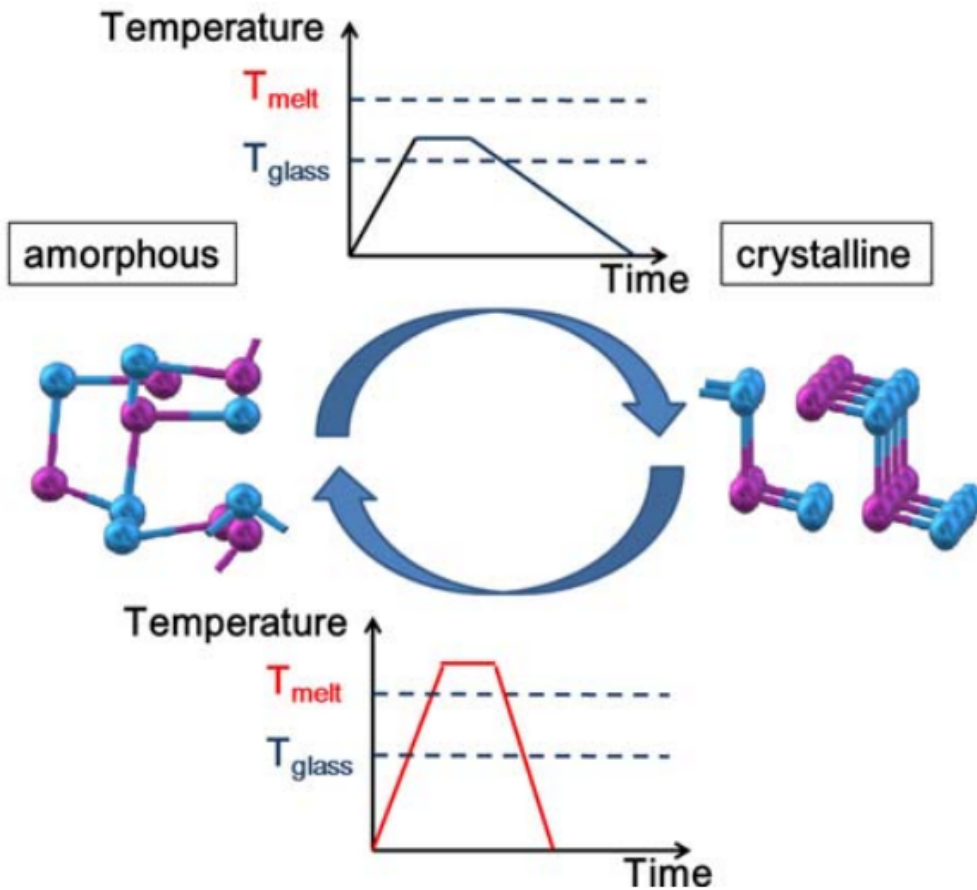


Figure 3.7: Schematic of thermal-induced transformation occurring mutually between amorphous and crystalline states. Figure taken from [22]

To read the memory, the applied voltage is lower than the one used for writing, in order to measure the resistance of the material without inducing a phase change [23]. Phase change memories technology needs two main characteristics:

- the thermal confinement to avoid heat dissipation in the surrounding of the memory cell;
- the reduction of the energy consumption due to the high current density needed to reach the melting point.

A promising strategy is again the nanostructuring of the material because it can bring a reduction of the crystalline thermal conductivity, so that heat will remain within the memory cell and be more effective in increasing the local temperature. The consequence will be the decrease of the programming current needed and thus of the energy losses. Therefore also in this application we can see how understanding heat transport in nanostructured GeTe is important.

3.4 Sample production

Our GeTe specimens are produced by the CEA-LETI research group using the sputter deposition technique which is a PVD (physical vapor deposition) method of thin film deposition. In this process the material is vaporized from a surface called target through a sputtering, that is a non-thermal vaporization of the material. The surface atoms of the target are physically extracted from the solid surface thanks to the energy transferred to them by a bombardment of atomic particles. This bombardment is usually generated by ions created by low pressure plasma and the particles detached from the target are deposited on the substrate, generating a thin film [24].

The sputter machine is made by an electrical circuit where the target is connected to the negative electrode and the component to be coated (substrate) is in the positive side of the anode (Fig. 3.8).

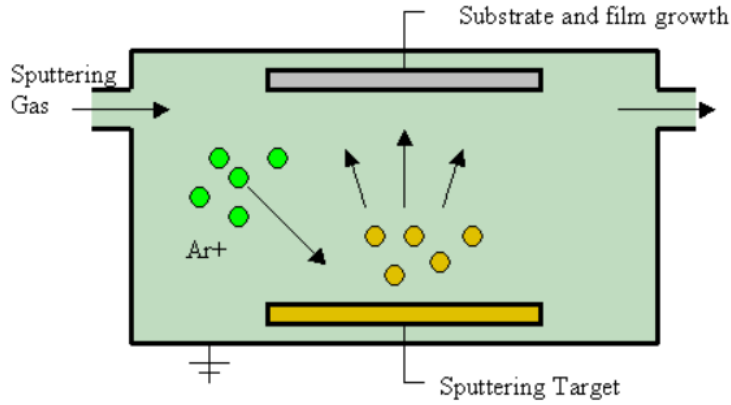


Figure 3.8: A schematic of sputter deposition

The method used by CEA-LETI is magnetron co-sputtering, where the magnetron is a high-power vacuum tube and co-sputtering means that two or more target (or “source”) materials are sputtered. The thickness and density homogeneity of the deposited layer are controlled by X-Ray Reflectivity and the Ge and Te compositions are measured by Rutherford Back Scattering (RBS) and Wavelength Dispersive X-Ray Fluorescence.

For our studies we also need GeTe-C samples, made by co-sputtering GeTe and C, which should have a strong thermal conductivity reduction compared to pure GeTe. GeTe-C nanocomposites are spontaneously formed by annealing the homogeneous amorphous GeTe-C thin film. Annealing the insulating amorphous system results in a crystallization which takes place at a higher temperature than in pure GeTe, accompanied by a phase separation, and leads to the formation of nanocrystalline grains of GeTe surrounded by amorphous carbon.

The films are capped by a 10 nm thick amorphous SiN or SiO_2 layer in situ in the deposition tool in order to avoid any surface reaction or oxidation in atmosphere.

3.5 State of the art of thermal and phonon measurements on GeTe thin film

In the literature, the study of the trend of phonons in GeTe nanocomposites has not yet been reported. A recent work has reported the experimental measurement of phonons in crystalline and amorphous GeTe using the picocooustic technique. The authors were able to estimate the speed of sound, which is very similar between the two phases, although slightly lower in the amorphous (~ 2400 m/s) [25]. However, they did not analyze the attenuation of phonons in the two phases.

My host group during this work (Valentina Giordano) had already published several theoretical works on the propagation of phonons in nanocomposites, proving that the presence of nanoinclusions can strongly reduce the average free path of the matrix material, inducing a crossover from propagative phonons to non-propagative phonons but with a diffusive nature. The consequence is that the thermal conductivity is decreased. The effect is greater when the contrast between the elastic properties of the two materials is stronger [26]. Depending on the wavelength of the phonons with respect to the size of the nanoinclusions and on the elastic contrast, different regimes can be identified: propagative, diffusive but also localized, corresponding to an entrapment of the vibrational energy between nanoinclusions or within them [27].

Starting from the possibility of the nanoinclusions to reduce the thermal conductivity, the aim of my thesis work is to develop an approach to measure the attenuation of the phonons on GeTe nanocomposites samples that will allow the future studies to understand the configurations of nanoinclusions that maximize the attenuation of phonons and therefore minimize the thermal conductivity.

Chapter 4

High frequency phonons detection methods

4.1 Detection strategy

The central topic of this thesis is the study of the propagation of single phonons in a nanomaterial. The presence of nanostructures will perturb the phonons consequently decreasing the thermal transport. To understand how nanoparticles influence the propagation of phonons, two characteristics must be measured:

- phonon velocity;
- phonon attenuation.

The measurements are first carried out on a bulk material to obtain the characteristics of the phonons which will then be compared with the measurements made on the nanomaterials. While velocity can be measured more directly, the attenuation measure deserves some considerations.

The attenuation of the vibrational motion (phonon) during propagation in the sample is caused by the energy loss at each interface (interfacial attenuation) and by the attenuation during propagation into the material itself (intrinsic attenuation). Starting from the attenuation measured, an additional calculation is thus needed to deduce the intrinsic attenuation, which describes how the phonon is perturbed by the material. For simplicity we will

use the energy loss rate (unity s^{-1}) γ ($= 1/\tau$), where τ is the phonon attenuation time (s). Since $\gamma_{measured}$ represents the attenuation measured through the experiments, it is possible to find $\gamma_{interfaces}$ and $\gamma_{intrinsic}$ through this relationship, which is nothing but a rewriting of the Mathiessen rule, seen previously:

$$\gamma_{measured} = \gamma_{interfaces} + \gamma_{intrinsic} \quad (4.1)$$

where $\gamma_{interfaces}$ is independent of the thickness of the material and $\gamma_{intrinsic}$ grows linearly with the thickness:

$$\gamma_{intrinsic} = \gamma_L \times L \quad (4.2)$$

where γ_L is the specific value per unit length. By measuring $\gamma_{measured}$ for the same material with different thicknesses we can plot the points on a cartesian plane which has the thickness of the sample L as X axis and $\gamma_{measured}$ as Y axis (Fig. 4.1):

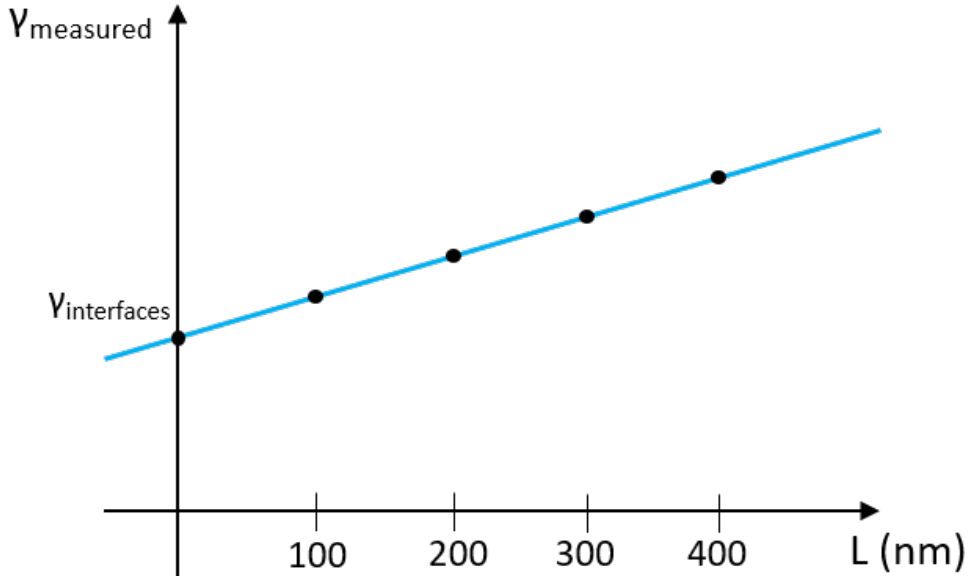


Figure 4.1: Attenuation as a function of sample thickness

We expect to find a straight line because $\gamma_{interfaces}$ is constant while $\gamma_{intrinsic}$ has a linear growth with the increase of L . The inverse of the angular coefficient of the line gives the intrinsic τ which is the attenuation of the

material per unit length. This value will be measured both in bulk homogeneous and in nanostructured materials to determine how the nanostructures affect thermal transport.

The intersection between the straight line and the axis of the ordinates directly gives $\gamma_{interfaces}$. This value tells how the energy lost at the interfaces affect phonon propagation.

It is possible to use advanced acoustic methods for measuring out-of-plane longitudinal-wave (phonons) modulus of thin films and their characteristics. The three main detection methods are:

- pulse echo method;
- phonon-resonance spectroscopy;
- Brillouin-oscillation method.

4.2 Pulse echo method

Using an ultrafast pulse laser (pulses around 100 fs), a strain wave is excited at the surface and propagates into the material. It then returns to the surface after the reflection on the sample/substrate interface generating a variation in the surface reflectance captured by the probe beam that we call "echo" [28] (Fig. 4.2).

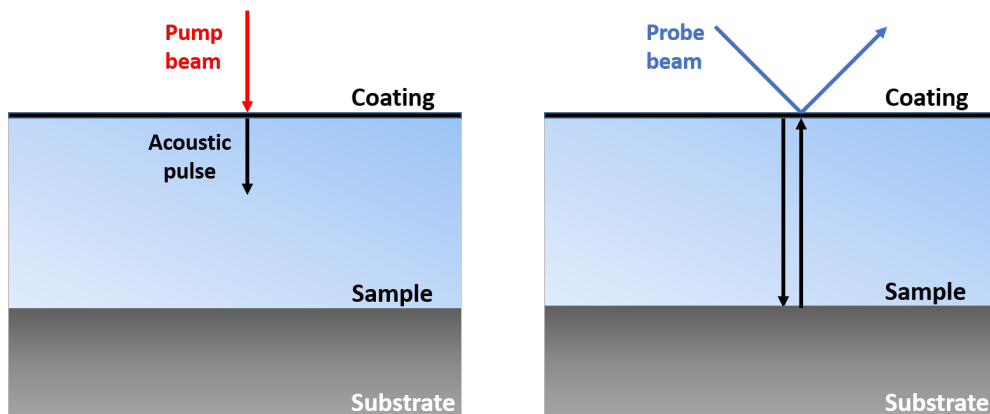


Figure 4.2: Schematic of the picosecond ultrasound pulse-echo measurement

The materials of the sample and the substrate must be chosen appropriately for the acoustic wave to be excited and to reflect at the GeTe-substrate interface. We can estimate it starting from the acoustic impedance Z , which is a measure of the ease with which a sound wave propagates through a particular medium:

$$Z = \rho \times v \quad (4.3)$$

where ρ is the density of the material and v is the speed of the sound wave in the material. From the acoustic impedances of the sample and the substrate we can evaluate the transmission coefficient T and the reflection coefficient R at the lower interface:

$$T = \frac{2 \times Z_1 \cos \Theta_1}{Z_1 \cos \Theta_1 + Z_2 \cos \Theta_2} \quad (4.4)$$

$$R = \frac{Z_1 \cos \Theta_1 - Z_2 \cos \Theta_2}{Z_1 \cos \Theta_1 + Z_2 \cos \Theta_2} \quad (4.5)$$

where Θ is the incidence angle. The higher the reflection coefficient at the sample/substrate interface the higher the change in the optical reflectance generated by the acoustic wave returning to the surface (echo amplitude). The round trip time Δt is measured to determine the sound velocity:

$$v = \frac{2 \times \Delta x}{\Delta t} \quad (4.6)$$

where Δx is the thickness of the sample.

With the pulse echo method it is possible to measure both the round trip time, which gives the sound velocity, and the amplitude of the echo, which gives the attenuation of the phonon.

This detection method can be used to measure the attenuation in materials using two different sample configurations:

- **With transducer** A thin metallic (Au, Pt, Pd, ...) coating purposely deposited on the top of the sample acts as a transducer and launches a longitudinal acoustic wave into the sample, whose frequency is related to the thickness of the coating (Fig. 4.3). The phonons propagate into the sample and return to the transducer after a reflection on the substrate, thus modifying its optical reflectivity. The advantage of this configuration is the possibility to tune the frequency of the propagating

phonon, which is set by the fundamental breathing mode frequency of the transducer (dependent on its thickness). This configuration is preferred when the sample is transparent (low absorption coefficient) but can be used also with opaque materials.

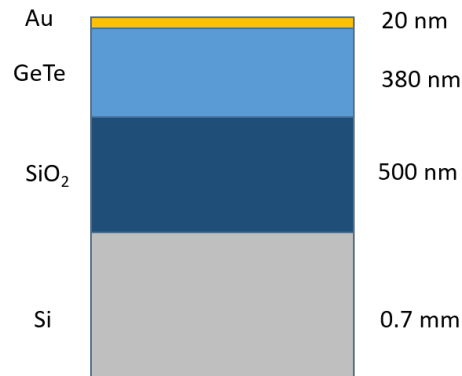


Figure 4.3: Sample geometry with transducer

- Without transducer** Alternatively, in the case of absorbing samples we can excite the sample directly without a transducer (Fig. 4.4): if the optical penetration length of the pump laser pulses is much smaller than the sample thickness, then the process will be equivalent and an echo may be detected because the first part of the sample acts as a transducer. This configuration can be used only for opaque materials (high absorption coefficient) in which the penetration length is small. If the transducer is not present, a SiO_2 layer with negligible thickness is used as coating layer and applied over the sample to protect the surface from deterioration.

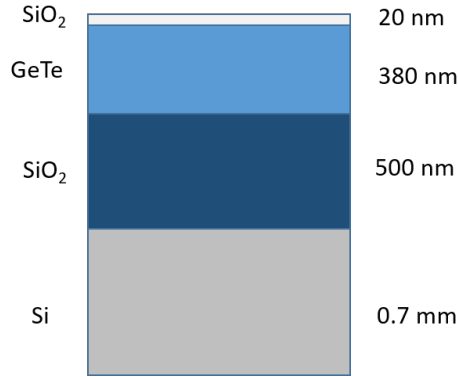


Figure 4.4: Sample structure without transducer

4.3 Phonon-resonance spectroscopy

To detect the echo with the pulse-echo method it is necessary that the layer has a sufficiently large thickness in order to locally generate the strain wave and let it propagate and reflect at the sample/substrate interface. In fact, if the film is thicker than approximately 70 nm echoes can be detected. If the film is thinner than 40 nm (ultrathin films) the pulse-echo method is no more exploitable as the whole sample will be reasonably excited by the pump pulse, which induces an homogeneous dilatation of the sample and excitation of its fundamental and harmonic acoustic thickness vibrational mode (Fig. 4.5).

In the case of a free-free interface, which is justified as the acoustic impedance of both air and substrate is lower than the one of the sample, the frequency of the vibrational mode is given by:

$$f_m = \frac{m}{2d} \sqrt{\frac{C_{33}}{\rho}} \quad (4.7)$$

where C_{33} is the out-of-plane longitudinal wave elastic modulus, ρ is the mass density of the film, d is the thickness and m is the order of resonance. As $\sqrt{\frac{C_{33}}{\rho}}$ is the longitudinal sound velocity:

$$v = \frac{2d \times f_m}{m} \quad (4.8)$$

Here there is a scheme of this detection method:

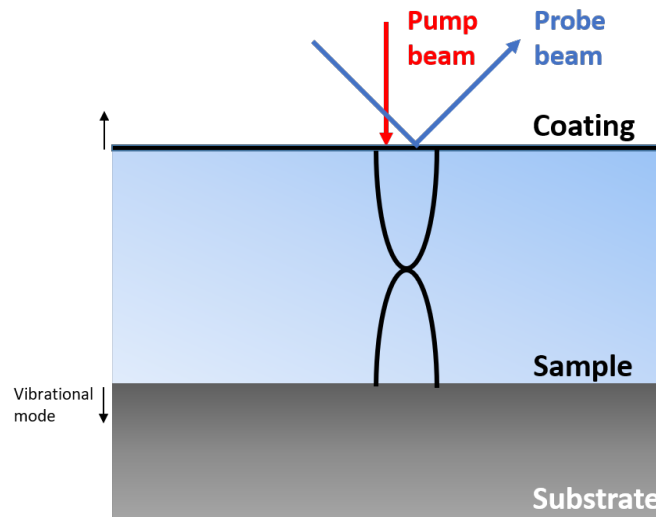


Figure 4.5: Schematic of the picosecond ultrasound phonon resonance spectroscopy

4.4 Brillouin-oscillation method

This method is based on Brillouin scattering which indicates the interaction of light with the material waves in a medium. As in the pulsed-echo technique, a thin film pump-light-absorbing optoacoustic generator (the transducer) is located at the interface between a sample and the air to launch the coherent acoustic strain waves into the transparent sample.

This method relies on the detection, by an optical time-delayed probe pulse, of the interference between the light reflected by the air/sample interface and the light reflected by the propagating acoustic wave (Fig. 4.6).

The measured signal varies with time because the relative phase of the light scattered by the acoustic wave and reflected by sample surface continuously varies with time due to the shift in the spatial position of the sound wave. If it propagates at a constant velocity in a spatially homogeneous medium, the phase difference between the interfering light fields changes in time linearly causing sinusoidal variations in the signal amplitude at a frequency called the Brillouin frequency. The acoustically-induced oscillating contribution to

the reflectivity signal is commonly known as the Brillouin oscillation.

In the first order approximation for strain, the oscillation frequency f_{BO} of the time-resolved optical signal is linked to the propagating sound velocity v through the Bragg's condition:

$$f_{BO} = \frac{2nv}{\lambda} \quad (4.9)$$

where λ is the wavelength of the probe light in the vacuum and n is the refractive index of the film at λ .

This method is interesting because it allows determination of both phonon propagation velocity (via the equation above) and attenuation, as it may be straightforwardly demonstrated that sound attenuation is directly given by the attenuation of the optical signal. Moreover no information of the film thickness is needed, and no need to detect the back echo of the acoustic wave. One limit is that this method can be used only for transparent samples which is not the case for GeTe, as it is based on the transmission of the probe pulse into the sample.

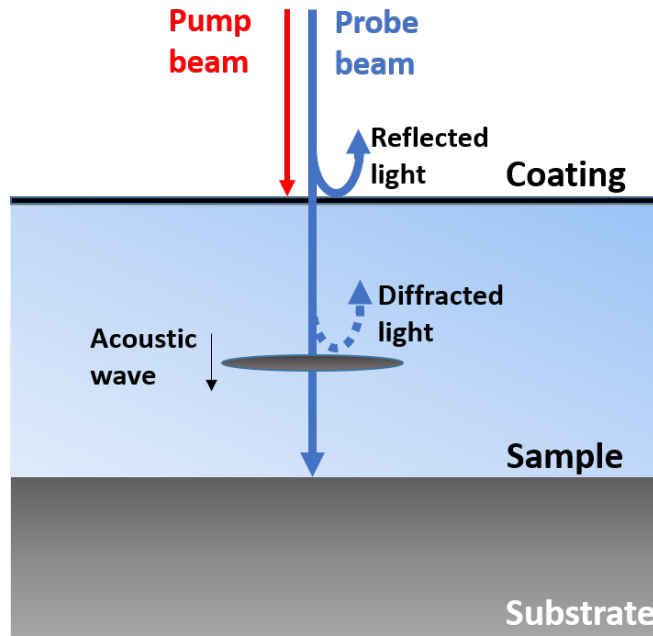


Figure 4.6: Schematic of the picosecond ultrasound Brillouin-oscillation method

4.5 Comparison between different methods

To summarize what mentioned in the previous sections, here are the main features of the three approaches:

	Measurement	Kind of sample
Pulse echo method	Phonon velocity and attenuation	Transparent (transducer needed) or opaque sample
Phonon-resonance spectroscopy	Phonon velocity	Thin sample
Brillouin-oscillation method	Phonon velocity and attenuation	Transparent sample

Table 4.1: A brief comparison of the detection methods introduced

With a closer look we note that the pulse-echo technique and the phonon resonance spectroscopy are different applications of the same principle:

- **Pulse-echo technique**
 - strong optical absorption;
 - short penetration depth;
 - excitation of a small fraction of the sample;
 - the generated pulse correspond to the superposition of the fundamental vibrational mode and many harmonics.
- **Phonon resonance spectroscopy**
 - weak optical absorption;
 - long penetration depth;
 - homogeneous excitation of the whole sample;
 - only the fundamental brethahnig mode is excited and detected.

More specifically, we refer to the phonon-resonance spectroscopy when the pump beam excites a non-negligible part of the sample thickness and consequently excites a few modes (ideally if the excited thickness exactly coincides with the sample thickness, only the fundamental harmonic would be excited). We refer to the pulse-echo technique when, through the use of the transducer or through the direct excitation on the sample (if the material is opaque), the pump beam excites a negligible layer of the material. This corresponds

to excitation of a very large number of harmonics generating an impulsive response that coincides with the echo that comes and goes. To understand this concept we can represent a Fourier series, that is a periodic function composed of a linear combination of sinusoidal functions:

$$f(x) = \sum_{k=1}^n \left(\frac{\sin(kx)}{k} + \frac{\cos(kx)}{k} \right) \quad (4.10)$$

For example this series with $k = 1$ (1 excited mode only) coincides with the pure breathing mode of the material (sinusoidal oscillation, Fig. 4.7):

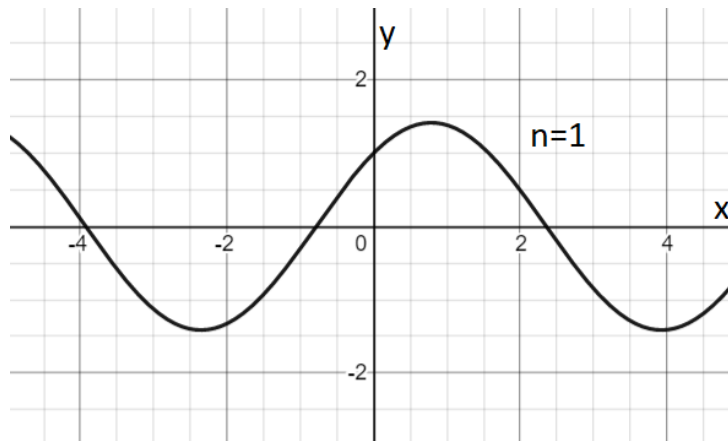


Figure 4.7: Fourier series of order 1

We note that increasing the number of stressed modes (large n) the signal becomes shorter (Fig. 4.8):

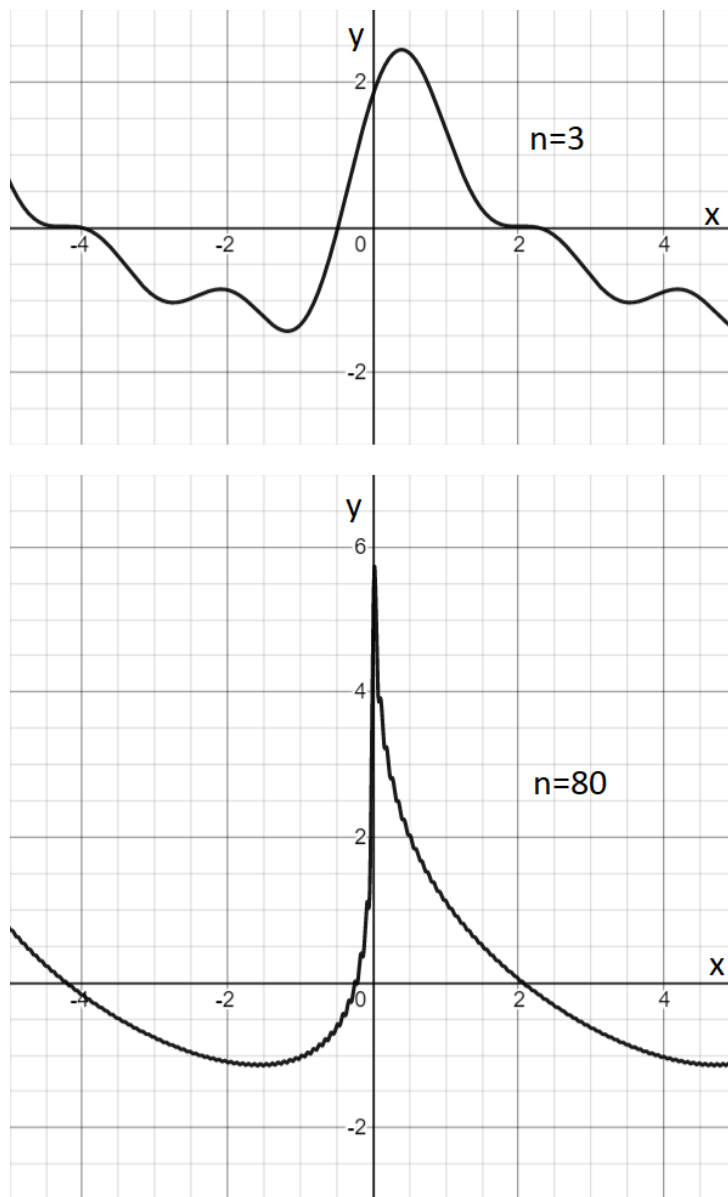


Figure 4.8: Fourier series of order 3 and 80

Observing a breathing mode of the material through the phonon-resonance spectroscopy or an echo through the pulse-echo method corresponds to the same physical phenomenon..

With the Brillouin-oscillation method, on the other hand, other effects are measured at, namely the interaction between an optical beam and the strain wave.

Chapter 5

Ultrafast acoustic pump-probe experiments

The ultrafast optical experiment involves the use of a femtosecond laser source (typically 100 fs pulses at 80 MHz repetition rate) which generates a beam that is divided into two beams: the pump and probe beams (Fig. 5.1).

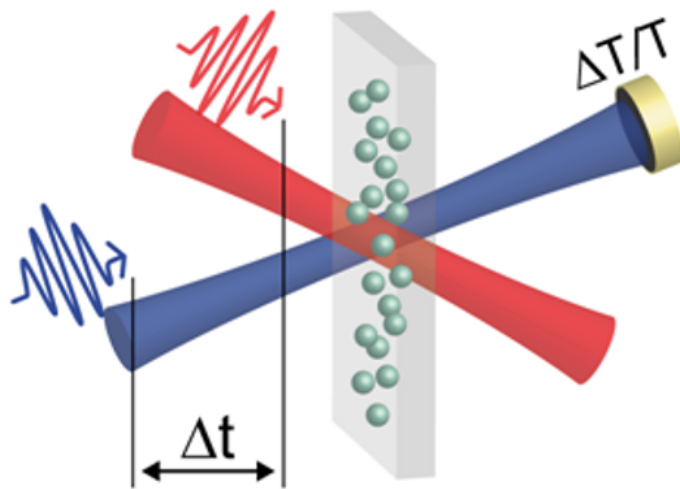


Figure 5.1: Basic principle of Pump and Probe. Image taken from [29] with author's permission.

The Pump beam is focused on the sample. The probe beam, after the re-

reflection on the sample, is collected by a photodiode. The pump pulse transiently modifies the probe optical reflectivity varying the material properties. By aligning the arrival time of the probe pulse (through a delay line composed by different mirrors placed on a rail), it is then possible to monitor the optical variations of the material properties with a very high (femtosecond) temporal resolution. The ultrafast acoustic pump-probe technique is applied for studying different transient ultrafast phenomena: coherent optical phonons and coherent acoustic phonons (CAP), carriers relaxation, spin dynamics, polaritons and thermal conduction. Coherent acoustic phonons are generated by the conversion of the optical energy of the pump pulse into mechanical energy [30]. A time-resolved pump-probe signal is shown in Fig. 5.2 on 40 nm gold nanoparticles in solution, with pump and probe wavelength equal to 900 and 450 nm respectively.

When the particles are excited, different physical phenomena are observed: light excitation-electronic motion coupling, electron-electron scattering, electron lattice energy transfers and acoustic vibrations. These phenomena take place in different timescales: the initial sharp peak (0-1 ps, Fig. 5.2) and decay reflect light- electron and electron-electron thermalization. Mechanical breathing of nanoparticles may induce optical oscillations (0-200 ps), while the longer monotonic decay (ns) is due to the thermal cooling of nanoparticles.

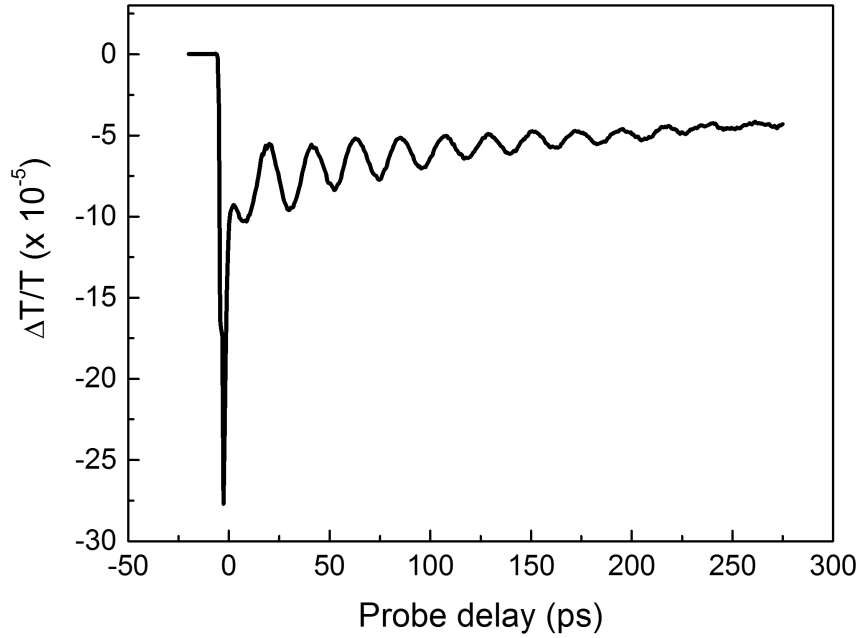


Figure 5.2: Experimental signal of a Ultrafast response of an Au nanoparticle. Image realized by Paolo Maioli (unpublished result).

As samples used for this work are opaque, we chose to detect reflected light by aligning the detection photodiode on the probe beam reflected by the sample.

5.1 Samples

For our experiments we used different types of samples mainly consisting of bulk GeTe (as in Fig. 5.3).

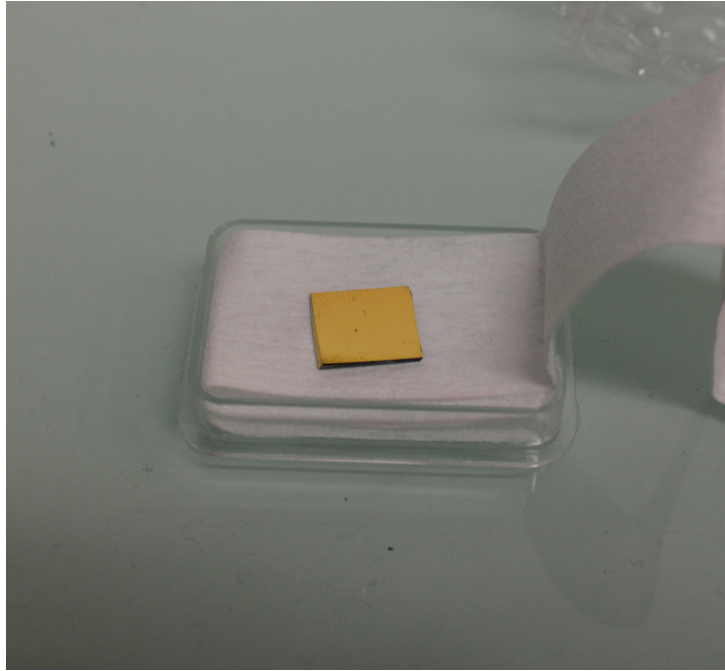


Figure 5.3: Picture of GeTe sample with Gold transducer used for measurements

We focused on bulk GeTe to have the response of the bulk material as a reference to later quantify modifications of the acoustic response due to inclusions of nanoparticles. The preliminary results obtained here will be extended in the future to GeTe nanocomposites. There are two types of sample:

- with transducer (made of gold, titanium or aluminum)
- without transducer

In the sample without transducer, a very thin transparent SiO_2 protective layer is present and can be neglected in the analysis of acoustic properties (Fig. 5.4).

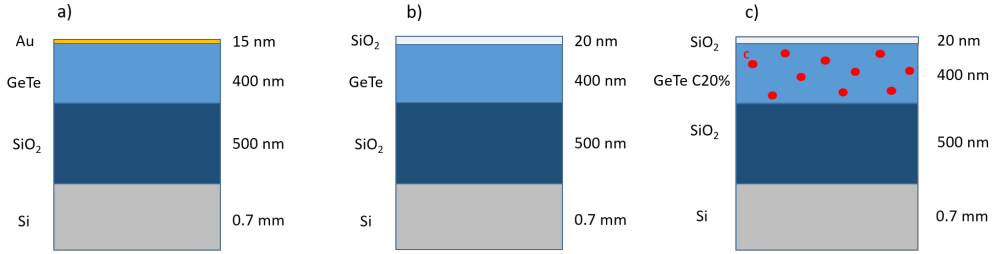


Figure 5.4: Different types of sample: a) bulk GeTe with transducer; b) bulk GeTe without transducer; c) nanocomposite GeTe without transducer

Measurements were made by varying the thickness of the transducer and the thickness of the GeTe sample. In this table I list all the samples measured:

TRANSDUCER (nm)	SAMPLE (nm)	SUBSTRATE
Au 40	GeTe 400	<i>Si</i>
Au 15	GeTe 200	<i>SiO₂</i>
Al 20	GeTe 200	<i>SiO₂</i>
Ti 20	GeTe 400	<i>SiO₂</i>
no	GeTe 100	<i>SiO₂</i>
no	GeTe 400	<i>SiO₂</i>
no	GeTe 800	<i>SiO₂</i>
no	GeTe + C20 % 400	<i>SiO₂</i>

Table 5.1: List of all the samples measured

Optical properties of crystalline and amorphous GeTe, important for the analysis of time-resolved optical signals, are reported in Fig. 5.5.

Real and complex optical indexes are reported in Fig. 5.5.a. The larger value of imaginary index k for crystalline with respect to amorphous material reflects the stronger optical absorption of the material with ordered lattice compared to the one with the amorphous (glass) structure. This also appears in the comparison of the absorption coefficient α , defined as $T = \exp(-\alpha L)$ (T being the transmission and L the material thickness), of the crystalline and amorphous GeTe (Fig. 5.5.b).

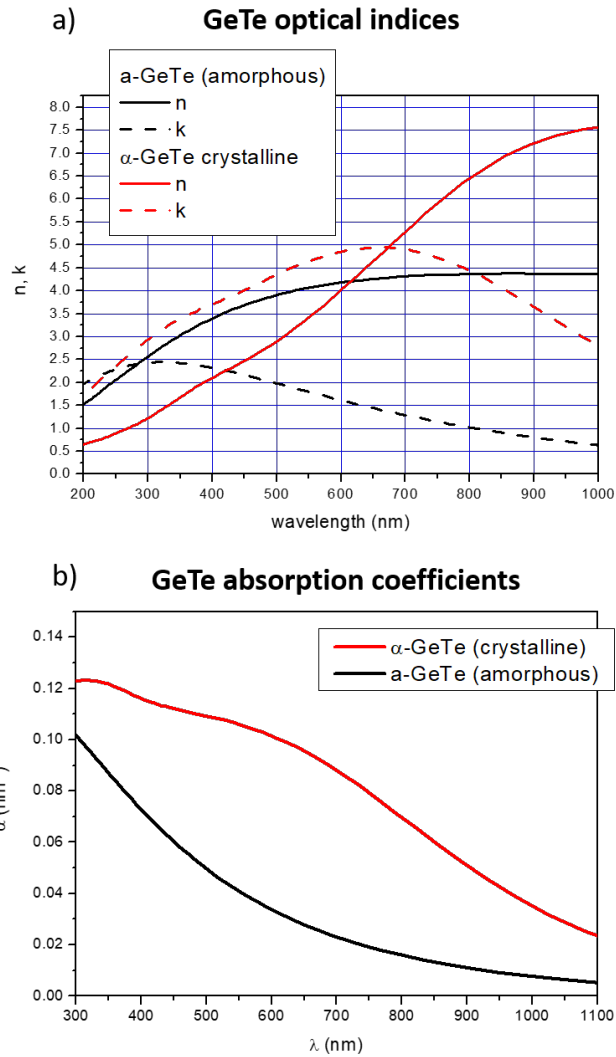


Figure 5.5: a) GeTe Optical index and b) GeTe absorption coefficient as a function of wavelength

5.2 Experimental set-up

I made measurements using two different set-ups, both developed at Institut Lumière Matière (Fig. 5.6). The configuration is similar: they differ only in the presence of an OPO (Optical Parametric Oscillator) in the set-up n°2

which facilitates the selection of the probe wavelength on a large range.

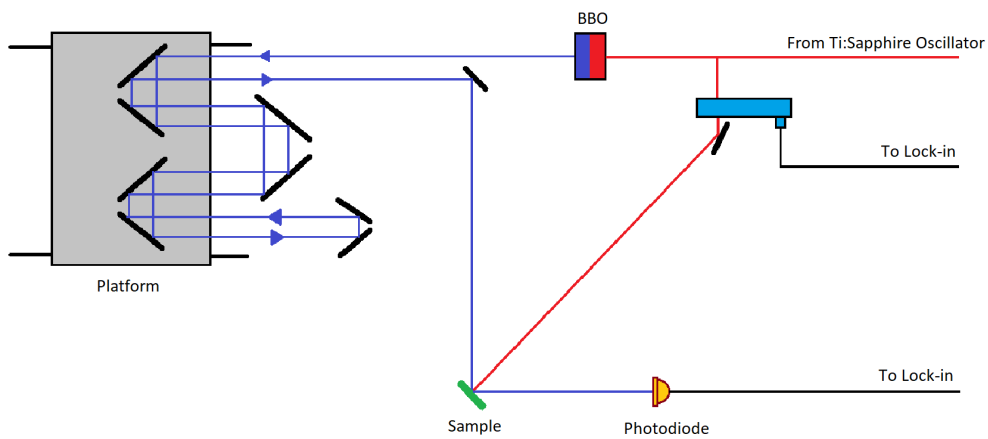


Figure 5.6: Pump and Probe set-up

5.2.1 Set-up n°1

Femtosecond infrared laser pulses are generated by a Ti-sapphire oscillator excited by a continuous laser source (Mira and Verdi by Coherent, shown in Fig. 5.7).

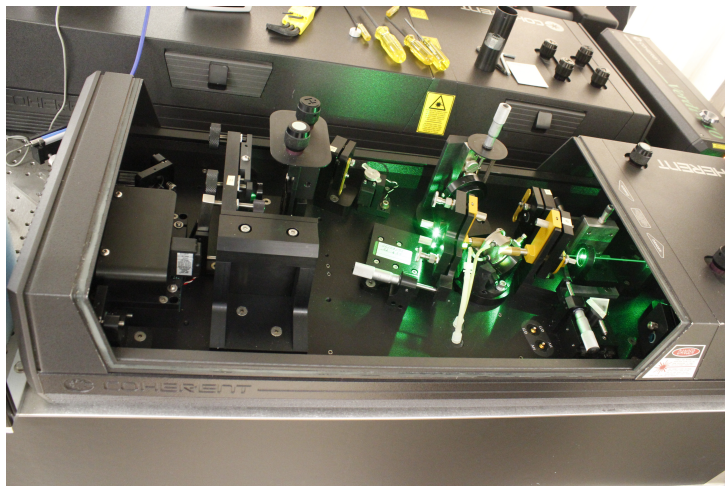


Figure 5.7: Coherent Verdi V10 laser source

The emission from the oscillator is then separated with a beam splitter to generate two different beams: the pump beam and the probe beam. The pump beam has an infrared wavelength around 900 nm, instead, the probe beam is frequency doubled to obtain a blue pulse (450 nm wavelength) with a Beta Barium Borate non-linear crystal (BBO). The delay between pump and probe pulse is precisely tuned by controlling the lengths of the optical paths of the two beams, from their separation with a beam splitter after the laser output until recombination on the sample. By mounting some mirrors on a movable mechanical delay line (shown in Fig. 5.8), the total path of one of the two beams can be precisely controlled and swept via a computer. As an order of magnitude, increasing the length of one of the two paths by 30 cm corresponds to introducing a delay of 1 ns.

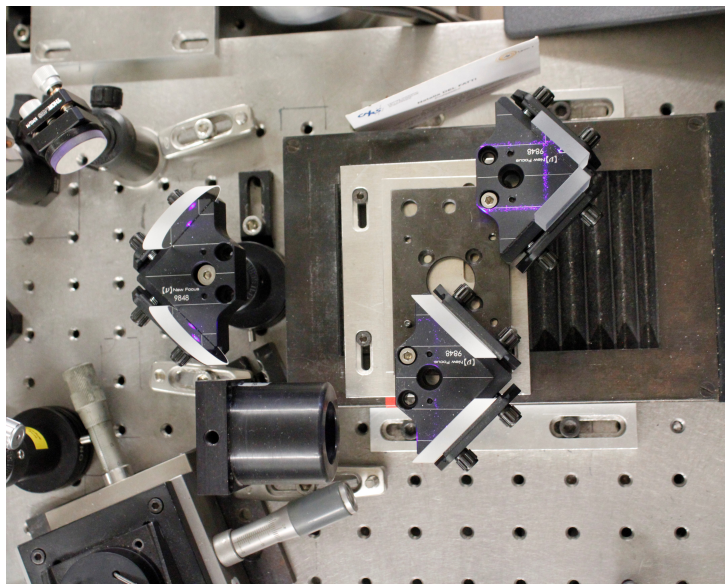


Figure 5.8: Delay line composed by different mirrors placed on a rail

To prevent the beam from moving sideways during the translation of the platform, an alignment optimization is done using a beam profiler to monitor the position of the probe beam after reflections into the movable mirrors. After moving the platform, the probe beam is focused on the sample with a lens (Fig. 5.9) and reflected to the photodiode (Fig. 5.10).

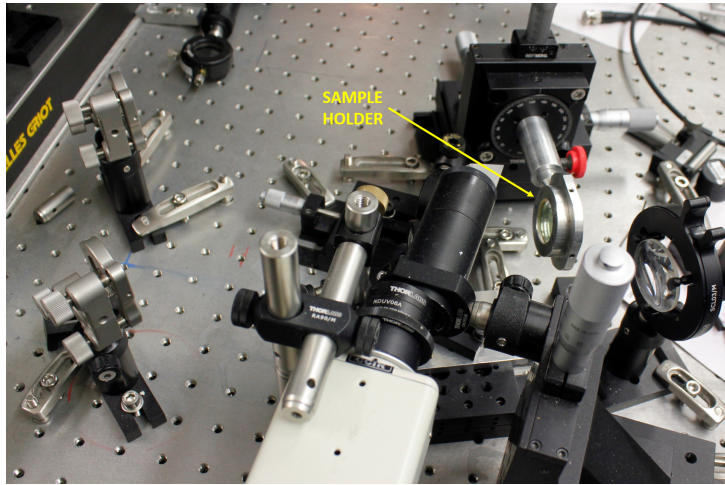


Figure 5.9: Final part of the experimental set-up with sample holder which reflects the probe beam and directs it to the photodiode

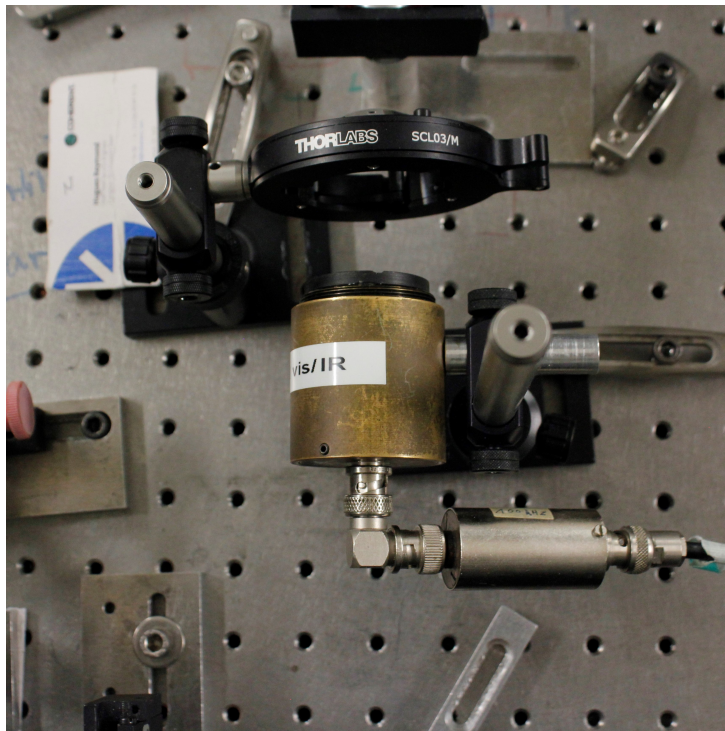


Figure 5.10: Photodiode which detects the beam focused by a lens

The pump beam, before reaching the sample, passes through a mechanical chopper (working range 5-100 kHz, shown in Fig. 5.11) which modulates the

intensity of the light beam and, used in combination with a lock-in amplifier, is used to improve the signal-to-noise ratio. The role of the lock-in amplifier will be explained better in a subsequent section.

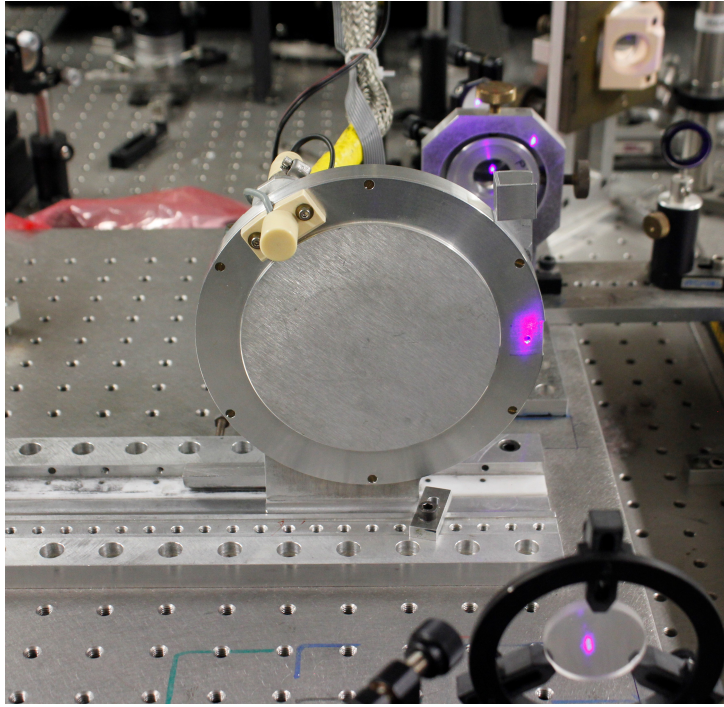


Figure 5.11: Mechanical Chopper

The pump power on the sample is around 50 mW, corresponding to an energy of 0.5 nJ per pulse. The probe power on the sample may vary over a wide range, from 0.5 to 10 mW. Two possible configurations are used, corresponding to different pump-probe delay ranges and probe pulse energies:

- **Long-delay configuration** The translation stage has a limited range, typically of 5 cm. By multiplying the number of reflections, we may extend the time delay range. Using many mirrors on the platform, it is possible to extend the measurements over a wider time window at the expense of the final power of the probe beam (Fig. 5.12). In fact, each mirror (in our case it is made of silver) has a reflection efficiency of about 0.9. In this configuration it is possible to cover a time window of around 1.3 ns ($\Delta T = \frac{8\Delta z}{c}$, being $\Delta z = 5\text{cm}$ the

maximum distance made by the platform, c the speed of the light and considering 4 reflections).

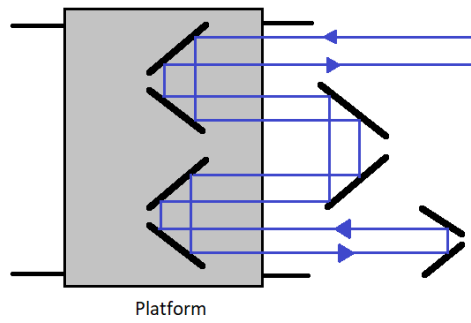


Figure 5.12: Long-time configuration of the set-up

- **Short-time configuration** Decreasing the number of mirrors reduces the time window but allows to keep a larger probe power and better signal over noise ratio (Fig. 5.13). In this configuration it is possible to cover a time window of around 350 ps ($\Delta T = \frac{2\Delta z}{c}$). Both long and short-delay configurations were used with this set-up.

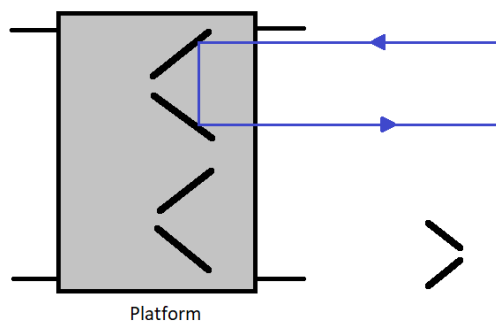


Figure 5.13: Short-time configuration of the set-up

5.2.2 Set-up n°2

In this set-up the femtosecond infrared laser pulses are generated by a Ti-sapphire oscillator excited by a continuous laser source (Mai-Thai system from Spectra-Physics). The second set-up has the same configuration of the first one except for the addition of an important component: the OPO (Optical Parametric Oscillator). It is a parametric oscillator that oscillates at optical frequencies. It converts an input laser with frequency ω_p into two output waves of lower frequency (ω_s, ω_i) by means of second-order nonlinear optical interaction. The sum of the output waves frequencies is equal to the input wave frequency: $\omega_s + \omega_i = \omega_p$. Only one of the two output waves (the one with higher frequency) is used while the other one (called "idler") is not. With the OPO, it is possible to vary more freely the wavelength of the pump (in the infrared or in the blue) or of the probe (covering all the visible from 500 to 700 nm). This is convenient to explore the optical response of different materials.

5.2.3 Lock-in acquisition

The relative transient modification of the optical transmission or reflection due to excitation of the sample by the pump pulse is typically very small ($\Delta R/R$ around 10^{-7} to 10^{-4}). To measure such a small change, a low noise technique based on a lock-in amplifier (Fig. 5.14) is necessary.

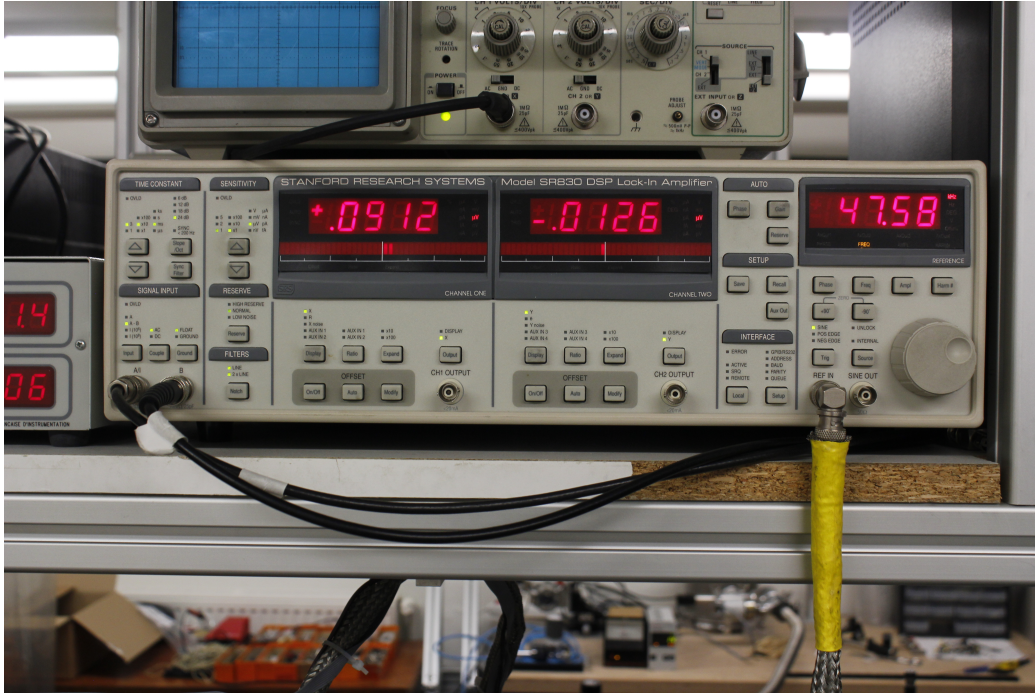


Figure 5.14: Lock-in amplifier

A lock-in amplifier extracts a signal from an extremely noisy environment. It is used to detect and measure very small AC signals providing a DC output proportional to the AC signal. The pump power is on/off modulated by a mechanical chopper, at frequency around 5 to 100 kHz. The electric signal from the photodiode is read by the lock-in amplifier, which filters out all the unneeded frequencies and only measures the component at the modulation frequency. With this technique, a very high signal over noise ratio is reached. It uses a technique known as phase-sensitive detection which operates by multiplying two signals together. The first signal is the input signal:

$$V_{in} = v_{sig} \sin(\omega_{sig}t + \theta_{sig}) \quad (5.1)$$

and the goal of the detection is measuring v_{sig} . The second one is a reference signal generated by the lock-in:

$$V_L = v_{ref} \sin(\omega_{ref}t + \theta_{ref}) \quad (5.2)$$

After the multiplication we obtain two AC signals, one at the difference

frequency $(\omega_{sig} - \omega_{ref})$ and the other at the sum frequency $(\omega_{sig} + \omega_{ref})$:

$$\begin{aligned}
V_{psd} &= v_{sig}v_{ref} \sin(\omega_{sig}t + \theta_{sig}) \sin(\omega_{ref}t + \theta_{ref}) \\
&= 1/2v_{sig}v_{ref} \cos((\omega_{sig} - \omega_{ref})t + \theta_{sig} - \theta_{ref}) + \\
&\quad -1/2v_{sig}v_{ref} \cos((\omega_{sig} + \omega_{ref})t + \theta_{sig} + \theta_{ref})
\end{aligned} \tag{5.3}$$

The cosine term with the sum frequency is removed by a low pass filter. Moreover the only DC component is for $\omega_{sig} = \omega_{ref}$ and is proportional to the amplitudes of the signals:

$$V_{psd} = 1/2v_{sig}v_{ref} \cos(\theta_{sig} - \theta_{ref}) \tag{5.4}$$

To sum up, the PSD and the low pass filter only detect signals whose frequencies are very close to the lock-in reference frequency. Noise signals at frequencies far from the reference are attenuated by the low pass filter and noise at frequency very close to the reference frequency will result in very low frequency AC output from the PSD ($|\omega_{noise} - \omega_{ref}|$ is small).

It is also possible to make $(\theta_{sig} - \theta_{ref})$ equal to zero. The output signal is shifted by 90° obtaining two different output: one proportional to $\cos(\theta_{sig} - \theta_{ref})$ and one proportional to $\sin(\theta_{sig} - \theta_{ref})$. If we call first output X and the second Y,

$$X = v_{sig} \cos(\theta_{sig} - \theta_{ref}) \quad Y = v_{sig} \sin(\theta_{sig} - \theta_{ref}) \tag{5.5}$$

X is called "in phase" component and Y "quadrature" component because when $(\theta_{sig} - \theta_{ref}) = 0$, X measures the signal while Y is zero. For this reason, to obtain the value of reflectivity we read only the X value which is the component in-phase with the pump excitation.

Chapter 6

Results

In this chapter are reported the measurements made with the ultrafast acoustic pump-probe set-ups. Only the most relevant experiments made on all the available samples are shown divided into the two sample morphologies: samples with transducer and without transducer.

In the case of samples with transducer, we expect to launch a strain wave by optical excitation of the thin transducer and detection of the pulse echo when the strain wave reaches the transducer after reflection on the opposite interface. In the case without transducer, the sample is directly excited. As already explained in chapter 4, the pulse-echo technique and the phonon resonance spectroscopy are two limiting cases of the same investigation technique. According to the excitation, homogeneous over the whole sample thickness or limited to the first nanometers, different vibrational modes may be excited. If the excitation is homogeneous (long penetration depth of the pump pulse) the fundamental breathing mode is selectively excited. In the case of a short penetration of the pump pulse, many thickness vibrational modes are excited, whose superposition gives a propagating strain wave. In all cases, we expect to observe a modulation of the optical signal, with a shape varying from a monofrequency oscillation (in the case of excitation of the fundamental breathing mode) to a more time-limited pulse-like oscillations, in the case of excitation of multiple modes.

6.1 Samples with transducer

I performed measurements on the samples with different types of transducers: Gold, Aluminum and Titanium. As already mentioned, the transducer is used to launch a longitudinal acoustic wave into the sample whose frequency is related to the thickness of the coating. The phonons propagate into the sample and return to the transducer after a reflection on the substrate.

Here are reported the normalized reflectance variation of the following samples (Fig. 6.1, 6.2):

- **GeTe (200 nm) with Gold transducer (15 nm) on Silica substrate**

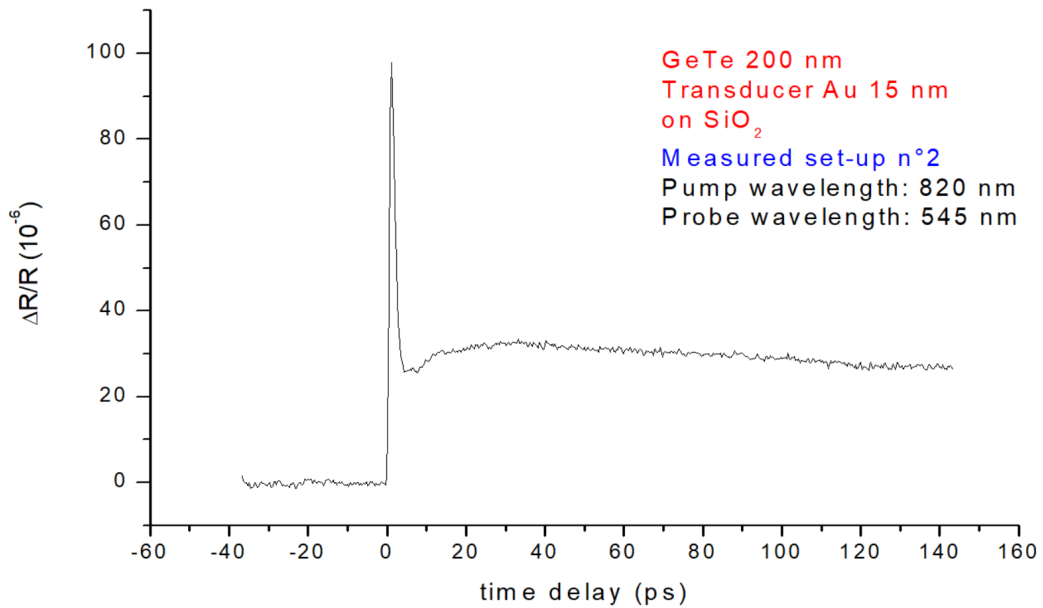


Figure 6.1: Relative optical reflectivity variation of a GeTe sample (200 nm) with a Gold transducer (15 nm) and Silica substrate

- GeTe (200 nm) with Aluminum transducer (20 nm) on Silica substrate

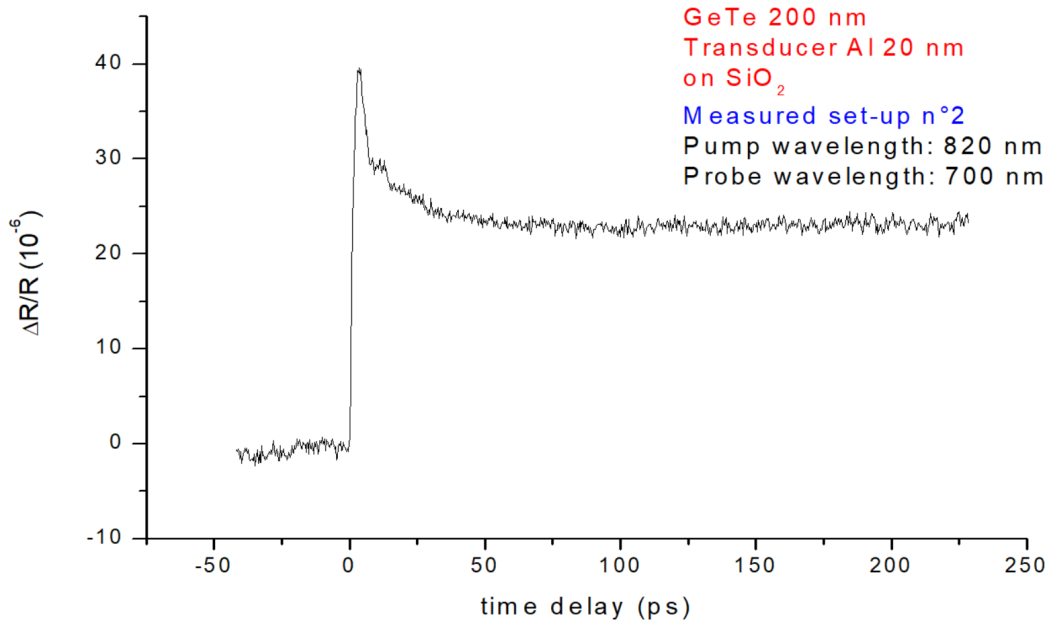


Figure 6.2: Relative optical reflectivity variation of a GeTe sample (200 nm) with an Aluminum transducer (20 nm) and Silica substrate

No echoes appear in the two signals shown above. Interestingly, a paper recently published on time-resolved pump-probe picoacoustic experiments on bulk GeTe reported observation of weak pulse echo in samples similar to the ones investigated [25]. We ascribe the difference in the results (no echos observed here) to some difference in the sample fabrication. Our samples probably present a roughness at the *GeTe/SiO₂* interface which induces additional energy loss and reduces the amplitude of the reflected acoustic wave.

In a measurement carried out on a sample with a Gold transducer, we observe the presence of an oscillation (Fig. 6.3):

- GeTe (400 nm) with Gold transducer (40 nm) on Silicon substrate

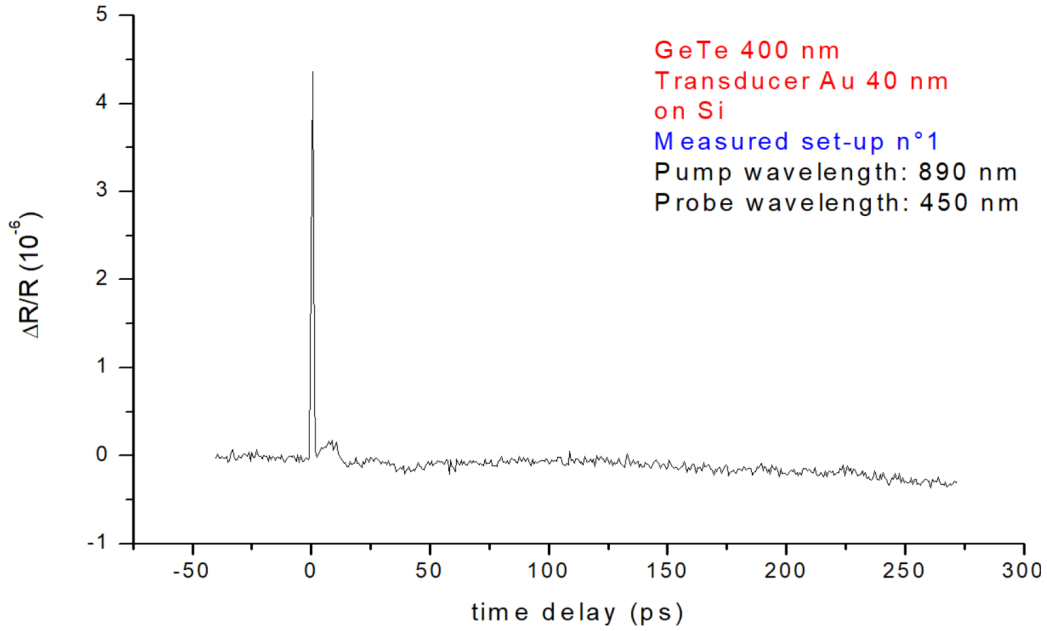


Figure 6.3: Relative optical reflectivity variation of a GeTe sample (400 nm) with a Gold transducer (40 nm) and Silicon substrate

An oscillation is present and it is ascribed to the breathing mode of the transducer. In fact, considering a sound velocity in Au of 3250 m/s, the period of the fundamental breathing mode is:

$$T = \frac{2 \cdot d}{v} = \frac{2 \cdot 40 \cdot 10^{-9}}{3250} = 24,6 \cdot 10^{-12} s = 24,6 ps \quad (6.1)$$

where d is the thickness of the transducer and v is the sound velocity. As is possible to see in the Fig. 6.3, there is an oscillation after the first peak which is in agreement with the calculated period. This optical oscillation has a period which approximately coincides with the period of the fundamental breathing mode of the transducer (Fig. 6.4), and thus does not bring information on the GeTe sample.

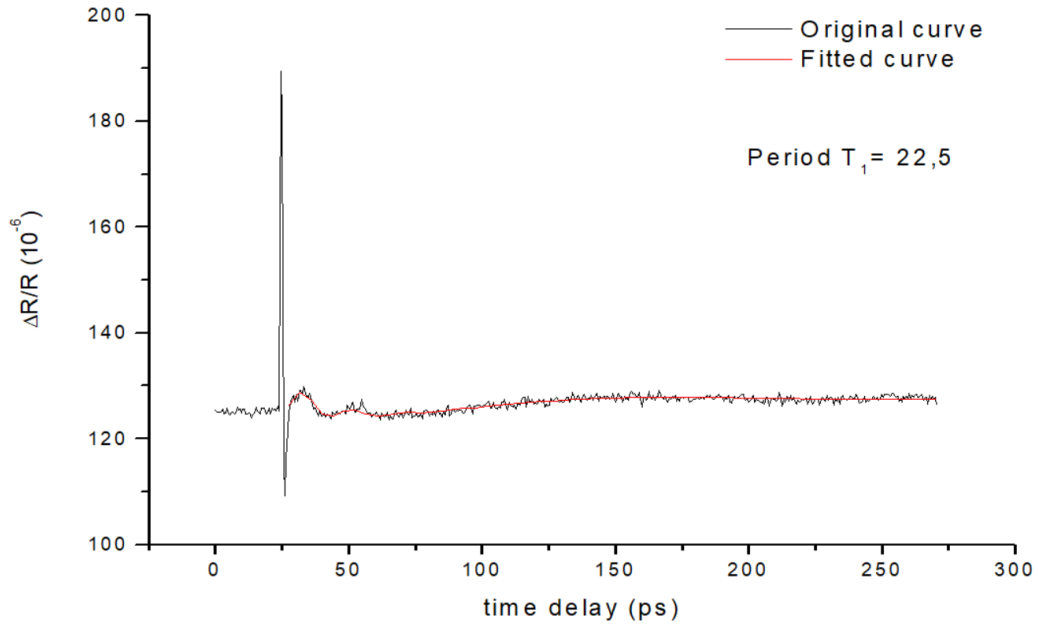


Figure 6.4: Fit of the relative optical reflectivity variation of a GeTe sample (400 nm) with Gold transducer (40 nm) and Silicon substrate. It is done to evaluate the period of the oscillation.

6.2 Samples without transducer

As mentioned before, it is possible to excite the sample directly without a transducer if the sample is opaque. In this case, the first part of the layer acts as a transducer. When the transducer is not present, a SiO_2 layer with negligible thickness is used as coating layer to protect the material, which does not affect the optical response, as it is transparent. Interestingly, some oscillations show up in the signals (Fig. 6.5 and 6.6).

- GeTe (100 nm) without transducer on Silica substrate

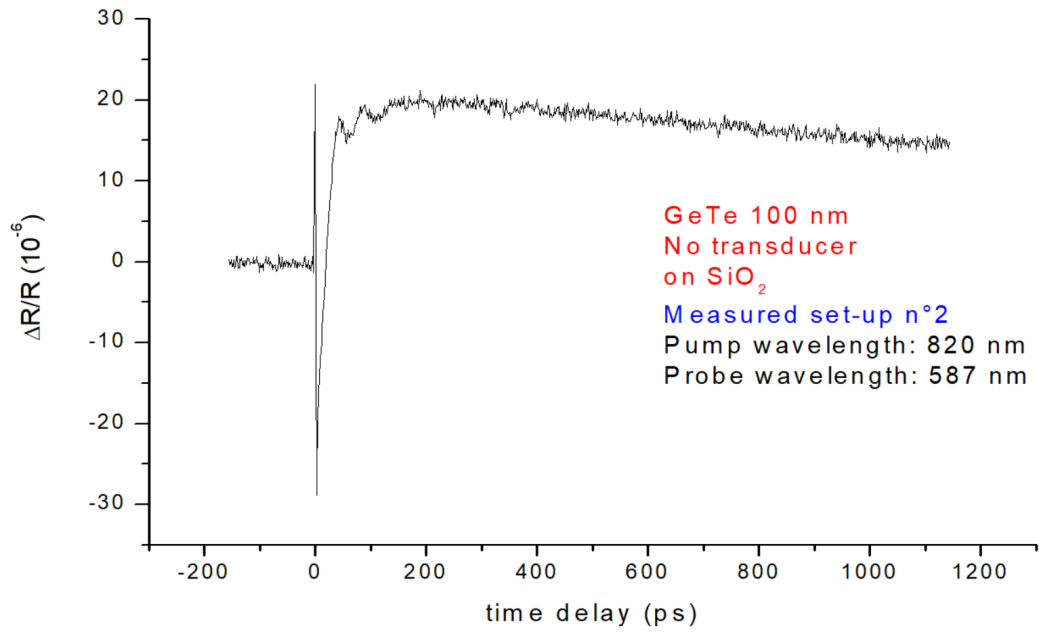


Figure 6.5: Relative optical reflectivity variation of a GeTe sample (100 nm) without transducer and Silica substrate

- GeTe (400 nm) without transducer on Silica substrate

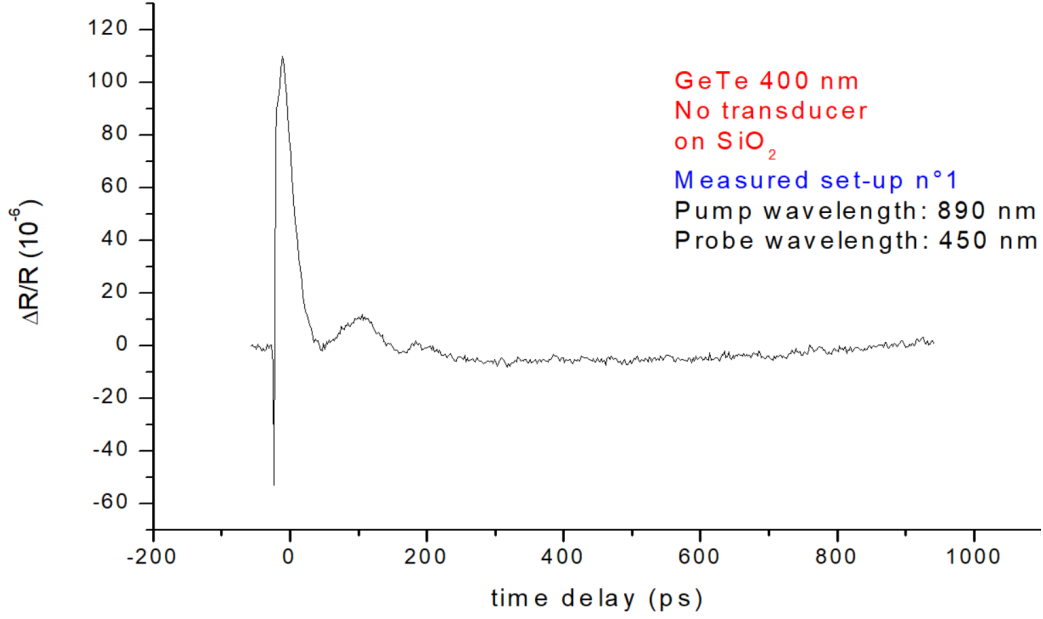


Figure 6.6: Relative optical reflectivity variation of a GeTe sample (400 nm) without transducer and Silica substrate

The oscillating part of the signal can be fitted as a sum of thickness vibrational modes, all with different frequencies, dependent on the harmonics order, and all sharing the same damping time (the hypothesis of a single damping time is actually a very strong simplification, on which we will comment later):

$$\frac{\Delta R}{R} = 10^{-6} \cdot \sum_n C_n \cos\left(\frac{2 \cdot \pi \cdot t}{T_1} + \phi\right) \cdot \exp^{-\frac{t}{\tau}} \quad (6.2)$$

where R is the optical reflectivity, C_n is the harmonic coefficient, T_1 is the period of the fundamental mode and ϕ is the phase.

In the case of breathing mode excitation only the fundamental $n=1$ mode is considered. The case of a propagating acoustic wave corresponds to the

equation with many i modes populated. This expression thus shows that the damping time τ , which is the main quantity searched here, can be deduced in both cases. As explained in chapter 4, an echo can be seen as a composition of a large number of harmonics. Since the attenuation of an oscillating signal is the same for each harmonic, the attenuation value obtained from the fit also corresponds to the attenuation of the echo.

Fits of these experimental curves using Eq. 6.2, after subtraction of the slow varying exponential contributions, are shown below (Fig. 6.7 and 6.8), together with the result of the fit. All the C_n , T_1 and τ values are affected by error bars of the order of $\pm 10\%$:

- **GeTe (100 nm) without transducer on Silica substrate**

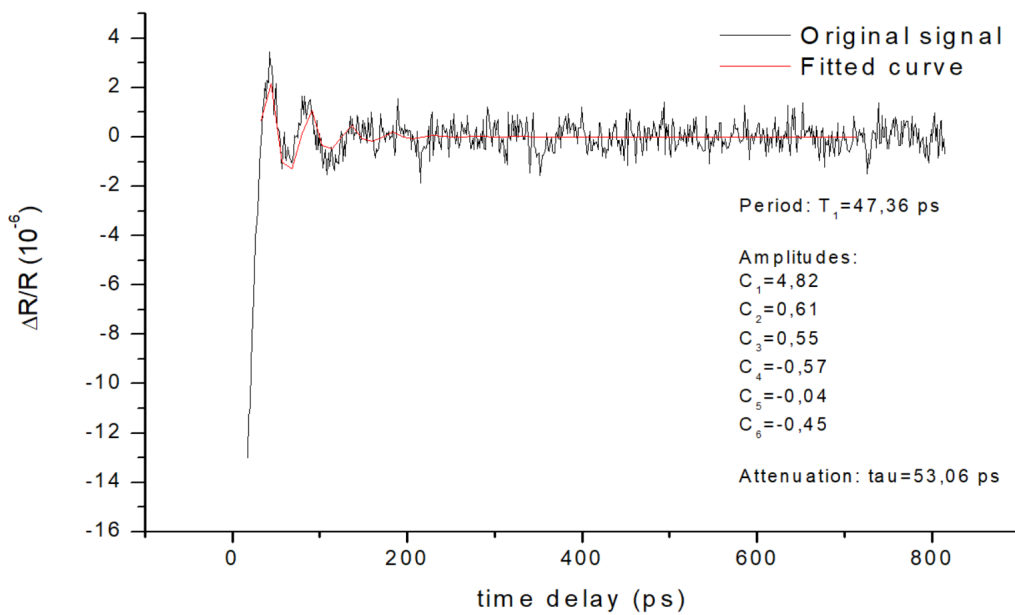


Figure 6.7: Fit of the relative optical reflectivity variation without the exponential component of a GeTe sample (100 nm) without transducer and Silica substrate.

- GeTe (400 nm) without transducer on Silica substrate

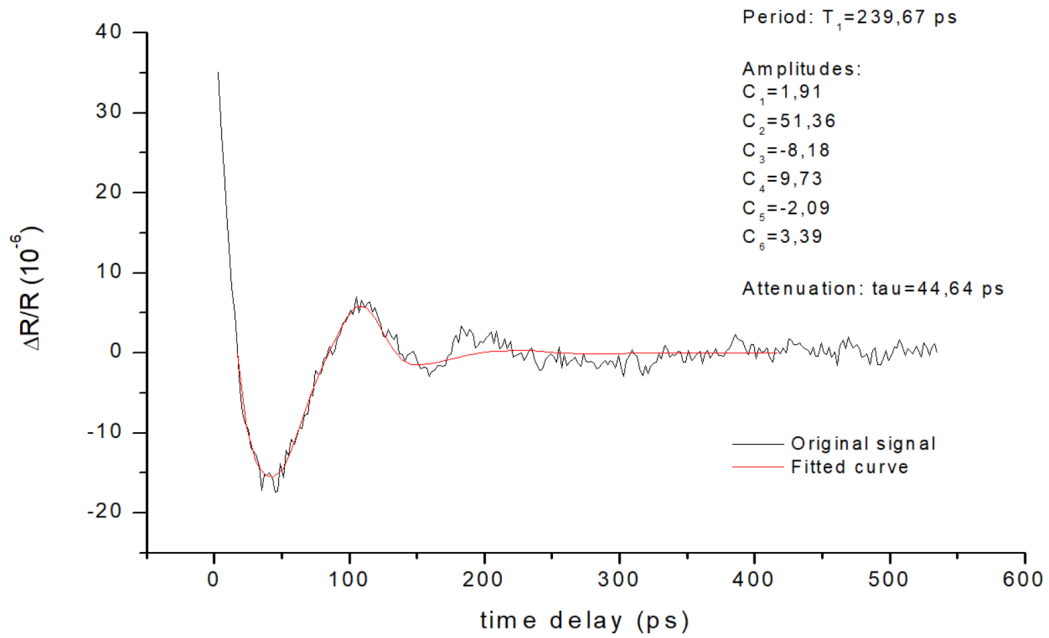


Figure 6.8: Fit of the relative optical reflectivity variation without the exponential component of a GeTe sample (400 nm) without transducer and Silica substrate

A graph with the amplitudes of first harmonics of the oscillating signals deduced by the fit is shown below (Fig. 6.9):

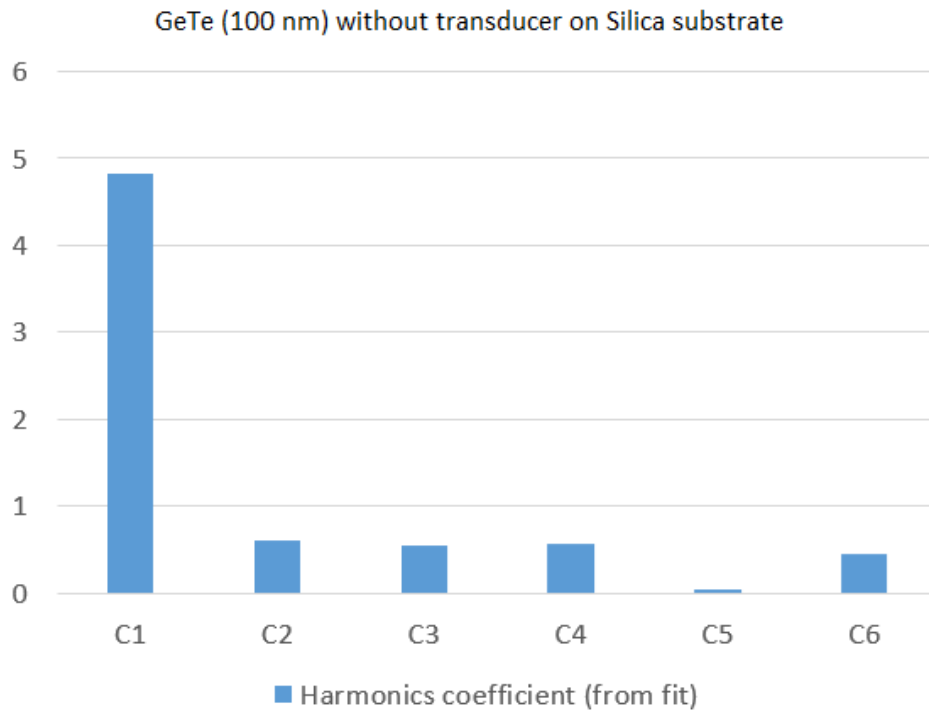


Figure 6.9: Plot of harmonics coefficient (absolute value) of a GeTe sample (100 nm) without transducer and Silica substrate.

As can be seen from the graph, the amplitude of the fundamental harmonic (first harmonic) is clearly larger than other amplitudes and this implies that the oscillation is essentially composed of the fundamental harmonic. This means that, in the case of this sample, the fundamental breathing mode is almost selectively excited.

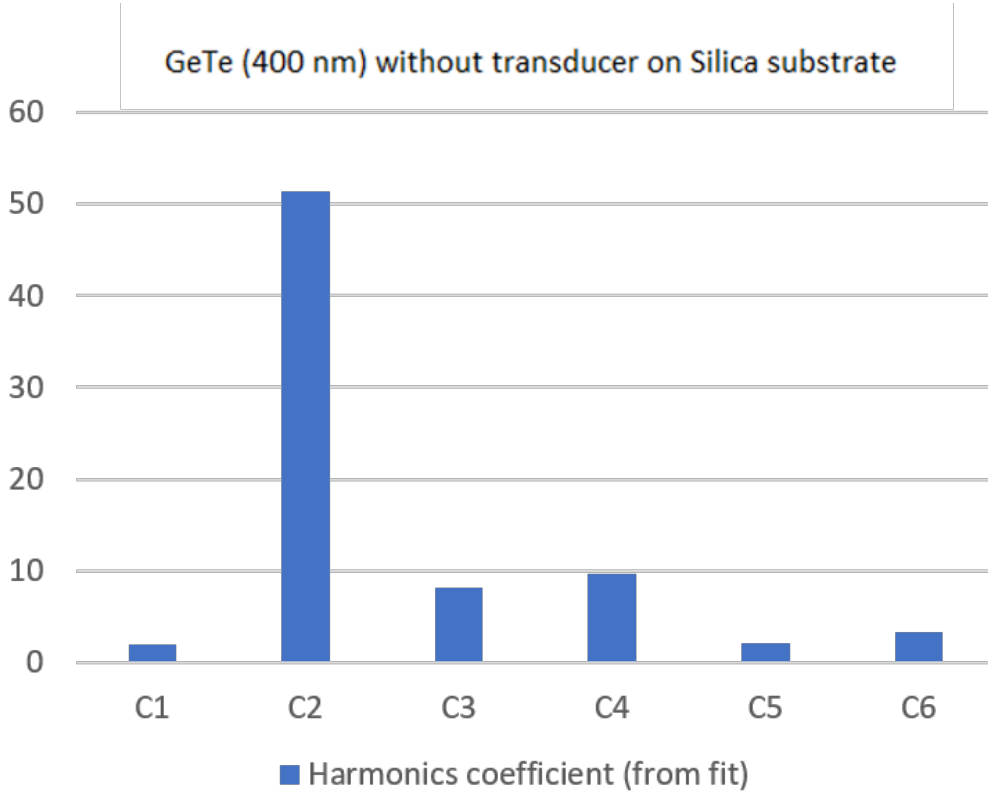


Figure 6.10: Plot of harmonics coefficient (absolute value) of a GeTe sample (400 nm) without transducer and Silica substrate.

In the case of the 400 nm thick GeTe sample, the amplitude of the second harmonic is the largest.(Fig. 6.10).

To reproduce the different harmonics contribution, we can consider that the excitation amplitude of each thickness vibrational mode is given by the overlap between the profile of the initial dilation induced by the pump pulse (ΔZ_{exc}) and the n-th displacement profile (ΔZ_n) of the vibrational mode n. This is expressed by the integral quantity:

$$C_n = \int_{-\frac{d}{2}}^{\frac{d}{2}} \Delta Z_n(z) \cdot \Delta Z_{exc}(z) dz \quad (6.3)$$

where z is the longitudinal coordinate along the GeTe layer (thickness d) with the origin of the axis in the center, ΔZ_n the normalized displacement field and ΔZ_{exc} the excitation profile.

- **Normalized displacement field ΔZ_n**

The normalized displacement field represents the eigenmodes of the GeTe layer (explained in detail in Appendix A). ΔZ_n varies according to whether it is present symmetric or anisymmetric mode:

If n is odd:

$$\bar{u}_n(z) = \sqrt{\frac{2}{d}} \sin\left(\frac{n\pi z}{d}\right) \quad (6.4)$$

If n is even:

$$\bar{u}_n(z) = \sqrt{\frac{2}{d}} \cos\left(\frac{n\pi z}{d}\right) \quad (6.5)$$

where \bar{u}_n is the normalized displacement field.

- **Excitation profile ΔZ_{exc}**

The excitation profile ΔZ_{exc} represents how the GeTe layer compresses and expands when subjected to laser pump excitation. A rough approximation is performed by assuming a linear displacement in the area of the sample where the photoinduced induced by laser pump excitation is present. The pump penetration depth can be computed from the Fig. 5.5 which reports the absorption coefficient, that is the inverse of the penetration depth: for a pump wavelength of around 850 nm the penetration depth is approximately 20 nm. Nevertheless, recent investigations reveal that the part of the energy deposited during the photoexcitation process takes place over a distance that clearly exceeds that defined by the skin depth. Indeed photocarriers (electrons) super-sonically diffuse in the crystalline GeTe over a distance that is around 7 times the optical skin depth, that is around 200 nm [25].

Therefore, we consier as a crude approximation of the excitation profile a dilation for the first 200 nm and no excitation for the remaining part of the sample depth (Fig. 6.11).

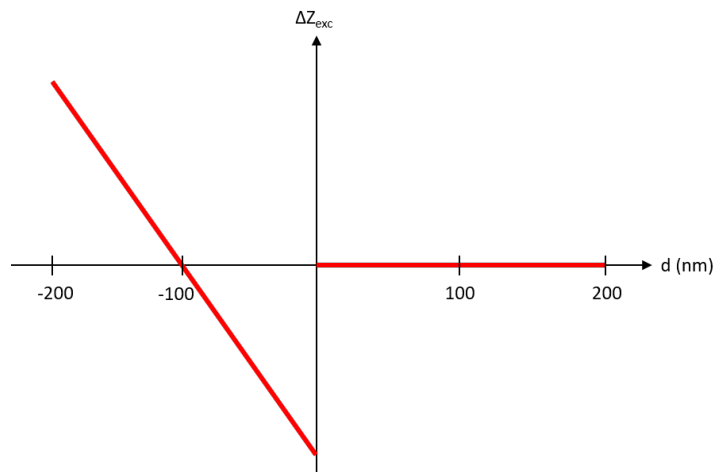


Figure 6.11: Approximation of the excitation profile of a 400 nm layer. The displacement present a dilation of the first 200 nm and no displacement in the remaining part.

By inserting the displacements in the Equation 6.3 it is possible to obtain the coefficients of the harmonics.

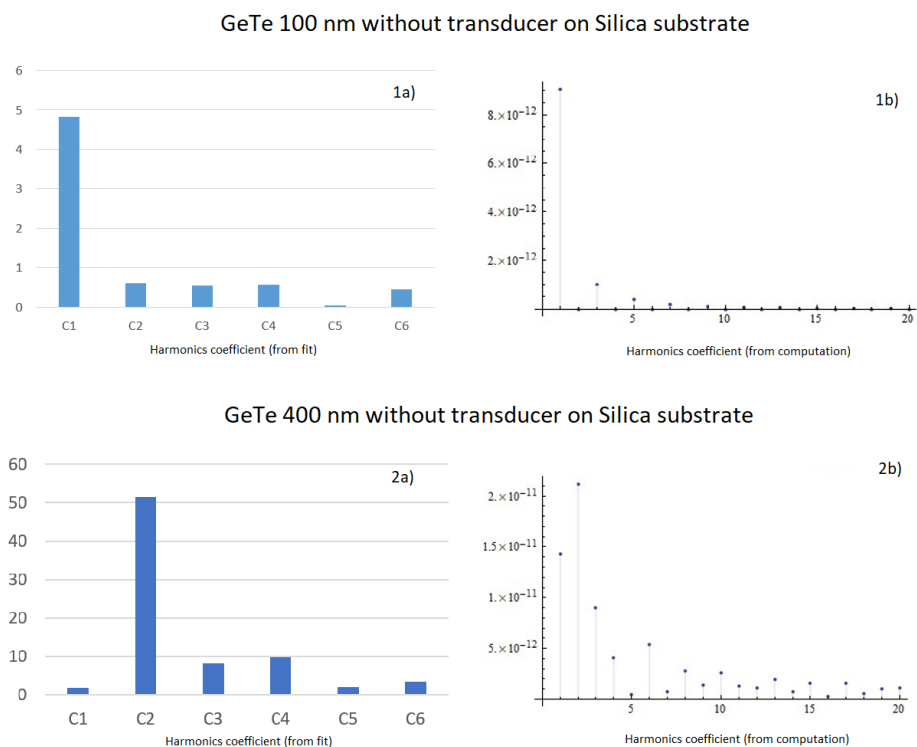


Figure 6.12: Plot of harmonics coefficient (absolute value $\times 10^{-6}$) deduced from the fit and from the computation above. 1a) and 1b) are referred to the GeTe sample (100 nm) without transducer and Silica substrate. 2a) and 2b) are referred to the GeTe sample (400 nm) without transducer and Silica substrate.

In the Fig. 6.12, 1a) and 1b) show the harmonic coefficients of the GeTe sample of 100 nm from the fit and the computation respectively. It may be seen that there is a good qualitative agreement between the two. The fundamental harmonic is predominant probably because, with a penetration of the excitation that can reach 200 nm, the whole GeTe sample (100 nm) is excited and therefore the breathing mode (fundamental harmonic) is dominant. Instead 2a) and 2b) show the harmonic coefficients of the GeTe sample of 400 nm. Here the agreement is good as for the predominance of the second harmonics, which has a period which is the half of the fundamental mode. This is thus consistent with an optical excitation on half of the thickness of the 400 nm sample. The good agreement between the amplitudes of the harmonics from the fit

and from the simplified model confirms the reliability of the fit of the oscillations and therefore the values of the attenuation τ obtained can be used to the intrinsic attenuation of the acoustic wave in the material, which is the main objective of this work. The measurements obtained are not sufficient to have a precise result but they allow to show the possibility of measuring the attenuation of the phonons. In the future, the same measurements will be performed on new samples to obtain more reliable results. This work is part of a preliminary phase a long-term project.

6.3 Attenuation analysis

Through this analysis, the damping time of the oscillations are:

- GeTe 100 nm without transducer on Silica substrate

$$\tau_{100} = (53 \pm 5) \times 10^{-12} s \quad (6.6)$$

- GeTe 400 nm without transducer on Silica substrate

$$\tau_{400} = (44 \pm 4) \times 10^{-12} s \quad (6.7)$$

As already explained in the Chapter 4, the attenuation of the vibrational motion is caused by the energy loss at each interface (interfacial attenuation) and by the attenuation during propagation into the sample (intrinsic attenuation). For the analysis it is more convenient to use dissipation rate, which is the inverse of the attenuation, γ ($= 1/\tau$). If $\gamma_{measured}$ represents the total attenuation measured through the experiments, the two contributions $\gamma_{interfaces}$ and γ_L sum up:

$$\gamma_{measured} = \gamma_{interfaces} + \gamma_L \times L \quad (6.8)$$

From the τ values deduced by the fits, we obtain:

- GeTe 100 nm without transducer on Silica substrate

$$\gamma_{measured,100} = \frac{1}{\tau_{100}} = 19 \times 10^9 s^{-1} \quad (6.9)$$

- GeTe 400 nm without transducer on Silica substrate

$$\gamma_{measured,100} = \frac{1}{\tau_{400}} = 22 \times 10^9 s^{-1} \quad (6.10)$$

Plotting these values on a cartesian plane which has the thickness of the sample L as X axis and $\gamma_{measured}$ as Y axis (Fig. 6.13):

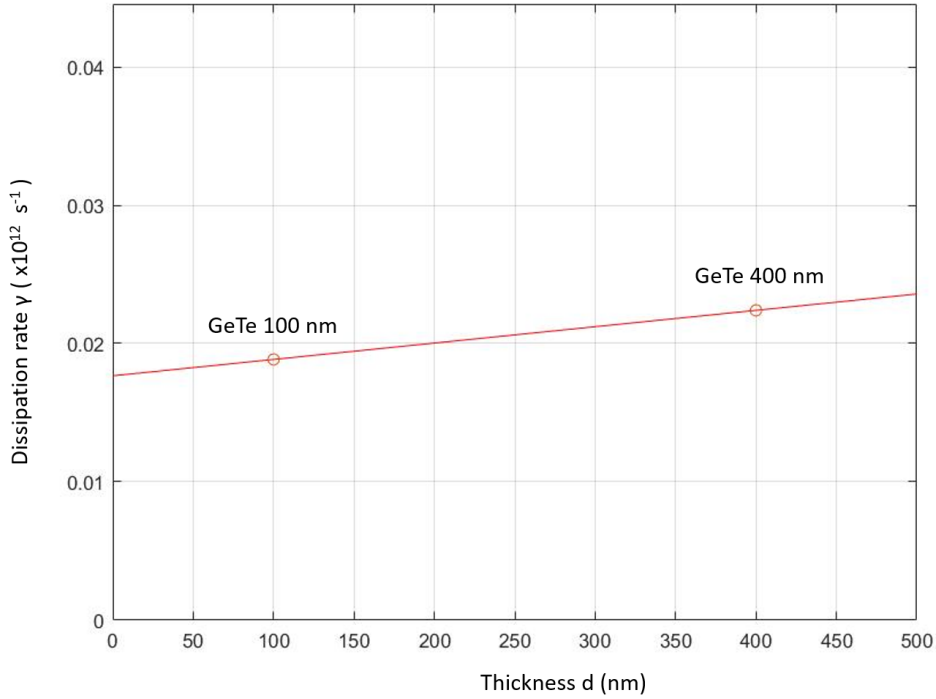


Figure 6.13: Plot of attenuation values obtained from fitted curve on a cartesian plane which has the thickness of the sample L as X axis and $\gamma_{measured}$ as Y axis

The linear fit shown in Fig. 6.13 gives:

$$\gamma_L = \frac{\gamma_{400} - \gamma_{100}}{d_{400} - d_{100}} = 1.0 \times 10^7 \frac{s^{-1}}{nm} \quad (6.11)$$

An additional value that can be obtained is $\gamma_{interfaces}$. Its value corresponds to the intersection between the straight line and the Y axis:

$$\gamma_{interfaces} = 18 \times 10^9 s^{-1} \quad (6.12)$$

This value represents how the interfaces between GeTe and Silica reduces the amplitude of the acoustic wave.

It is important to underline that these obtained values are very qualitative as they have been deduced with a very limited number of samples under some strong assumptions. In particular, more precise computations are needed to confirm the projection of initial photoinduced dilation on the harmonic modes displacements, thus confirming validity of this approach. More experiments and samples are needed to estimate a reliable value of the intrinsic damping γ_L . Nevertheless, these preliminary results seem to indicate that deduction of the intrinsic attenuation is possible starting from time-resolved experiments.

More importantly, the strongest assumption made here is the non-dependence of the attenuation on phonon frequency. This is actually not true in general. Depending on the dominant scattering mechanism, the attenuation can have a very strong dependence on the frequency (following a power law with exponent 2 up to 4). This means that the slope method in the attenuation vs thickness plot can only be applied if the phonon frequencies are similar. This is not the case here, where the dominant frequency is about 21 GHz for the 100 nm thin film and 8 GHz for the 400 nm thin film. In the future a more detailed sinusoidal decomposition with a frequency dependent attenuation needs to be used and only attenuations from the same frequencies can be compared through the thicknesses.

Chapter 7

Conclusions

In this work, thermal transport in nanostructured thin films is investigated employing Ultrafast time-resolved spectroscopy (pump and probe spectroscopy). A strain wave is launched by optical excitation and detected as a pulse echo or an oscillation of the sample optical reflectivity.

The oscillating part of the signal can be fitted as a sum of thickness vibrational modes, all with different frequencies, dependent on the harmonics order, and all sharing the same damping time. Since the attenuation of an oscillating signal is the same for each harmonic, analyzing the harmonics it is possible to measure the damping of oscillations for each sample. Comparing samples of two different thicknesses we found an intrinsic value for the phonon attenuation.

The full analysis which including all harmonic modes indicates that a visible echo in the time-resolved optical signal is not needed to retrieve the value of intrinsic attenuation, which can be inferred from the oscillating signals also in the absence of a defined echo.

Although the method needs to be further developed to account for the frequency dependence of the attenuation, it is already a proof of concept that the extraction of the intrinsic attenuation is possible. This method will be used in a more detailed study using samples of different thicknesses to obtain a more reliable value of strain wave attenuation and to be able to compare it with samples of different compositions.

Appendix A

Longitudinal vibrations of the sample

A.1 Slab model

It is possible to compute the normalized displacement field through a simplified model called "slab model" [31]. We consider a single slab made of an homogeneous linear isotropic and purely elastic material (GeTe in our case) defined by its mass density ρ and its longitudinal sound velocity v (Fig. A.1). The lateral extent of the slab is assumed infinite and thus the transverse and the longitudinal vibrational eigenmodes can be analyzed separately.

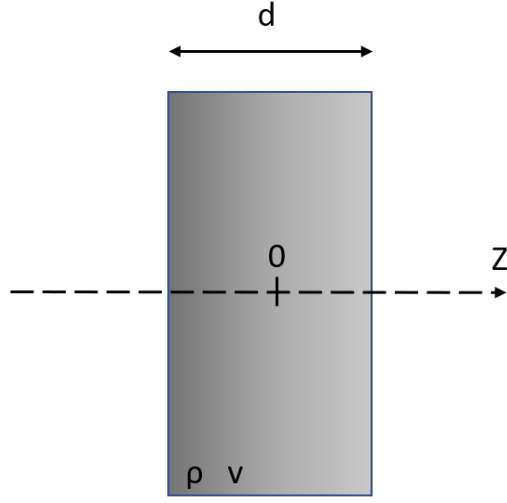


Figure A.1: A single slab of thickness d

$u(z, t)$ is the displacement field. Along the longitudinal direction z and neglecting the body force density, it is governed by the Navier's equation:

$$\frac{\partial^2 u(z, t)}{\partial t^2} = v^2 \frac{\partial^2 u(z, t)}{\partial z^2} \quad (\text{A.1})$$

Considering an harmonic solution, it is possible to rewrite the equation as:

$$\frac{\partial^2 u(z, t)}{\partial z^2} + \frac{\omega^2}{v^2} u(z) = 0 \quad (\text{A.2})$$

Moreover the stress component $t(x)$ is given for longitudinal motion by:

$$t(z) = \rho v^2 \frac{\partial u(z)}{\partial z} \quad (\text{A.3})$$

The solution of the equations A.2 and A.3 are:

$$u(z) = A \cos\left(\frac{\omega z}{v}\right) + B \sin\left(\frac{\omega z}{v}\right) \quad (\text{A.4})$$

$$t(z) = \rho v \omega [-A \sin\left(\frac{\omega z}{v}\right) + B \cos\left(\frac{\omega z}{v}\right)] \quad (\text{A.5})$$

The aim of this model is understanding the different eigenmodes. As the GeTe acoustic impedance ($Z = 21000 \text{ kg/s} \cdot \text{m}^2$) is higher than air impedance ($Z = 429 \text{ kg/s} \cdot \text{m}^2$) and Silica impedance ($Z = 12760 \text{ kg/s} \cdot \text{m}^2$), it is possible to simplify the model considering a stress-free condition in which

$t(\pm h/2) = 0$. Indeed stress-free boundary conditions are used for describing interfaces dividing the sample from a medium with a much smaller acoustic impedance.

The two boundary conditions lead to an homogeneous linear system of two equations. The eigenfrequencies are founded searching the zero of the determinant of the homogeneous linear system.

$$\sin\left(\frac{\omega d}{v}\right) = 0 \quad (\text{A.6})$$

$$\omega_n = n \frac{\pi v}{d} \quad (\text{A.7})$$

where n is an integer ≥ 0 .

There are three different groups of eigenmodes:

- **n=0** This mode corresponds to a rigid translation;
- **n odd** Normalized displacement field:

$$\bar{u}_n = \sqrt{\frac{2}{d}} \sin\left(\frac{n\pi z}{d}\right) \quad (\text{A.8})$$

These modes correspond to **symmetric modes** [$u_n(-z) = -u_n(z)$] (Fig. A.2).

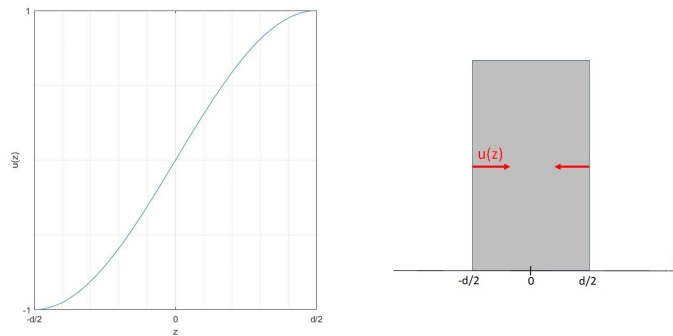


Figure A.2: (a) The normalized displacement field of symmetric modes (b) A depiction of the motion in the sample

This means that the displacement fields are symmetric relative to the x-y median plane at $z=0$.

- **n even** Normalized displacement field:

$$\bar{u}_n = \sqrt{\frac{2}{d}} \cos\left(\frac{n\pi z}{d}\right) \quad (\text{A.9})$$

These modes correspond to **antisymmetric modes** [$u_n(-z) = -u_n(z)$] (Fig. A.3).

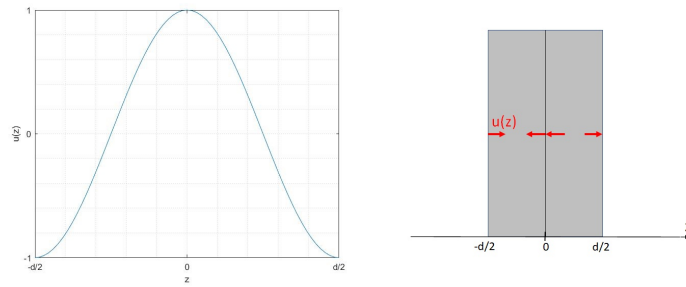


Figure A.3: (a) The normalized displacement field of anti-symmetric modes (b) A depiction of the motion in the sample

Bibliography

- [1] B. Khan K. Zeba, S.M. Alib. A survey on waste heat recovery: Electric power generation and potential prospects within Pakistan. *ScienceDirect*, 75:1142–1155, 2017.
- [2] SunKook Kim Seok-Ho Rhi Shiho Kim, Soonseo Park. A Thermoelectric Generator Using Engine Coolant for Light-Duty Internal Combustion Engine-Powered Vehicles. *Journal of Electronic Materials*, 40(5):812–816, 2011.
- [3] Alexander A.BalandinaDenis L.Nikaab. Phononics in low-dimensional materials. *Materials Today*, 15(6):226–275, 2012.
- [4] Charles Kittel. *Introduction to Solid State Physics*. John Wiley Sons, Inc.
- [5] Alexander Balandin. Thermal properties of semiconductor low-dimensional structures. *Phys. Low-Dim. Structures*, 2000.
- [6] Y. Takeda and T.P. Pearsall. Failure of Mattheissen’s Rule in the Calculation of Carrier Mobility and Alloy Scattering Effects in Ga_{0.47}In_{0.53}As. *Electronics Letters*, August 1981.
- [7] M. AsheghiKatsuo KurabayashiKatsuo KurabayashiR. KasnaviKenneth GoodsonKenneth Goodson. Thermal conduction in doped single-crystal silicon films. *Journal of Applied Physics*, 91:5079, 2002.
- [8] Guanjie Wang Yongda Huang, Jian Zhou and Zhimei Sun. Abnormally Strong Electron–Phonon Scattering Induced Unprecedented Reduction

- in Lattice Thermal Conductivity of Two-Dimensional Nb_2C . *American Chemical Society*, 141(21):8503–8508, 2019.
- [9] Jie Zoua and Alexander Balandin. Phonon heat conduction in a semiconductor nanowire. *Journal of Applied Physics*, 89:2932, 2001.
- [10] Patrick E. Hopkins. Dispersion considerations affecting phonon-mass impurity scattering rates. *Journal of Applied Physics*, 1:041705, 2011.
- [11] C. R. Tellier and A. J. Tosser. Size Effects in Thin Films. *Elsevier Scientific*, January 1982.
- [12] G. X. Zhai-et al. G. H. Tang, Y. Zhao. Phonon boundary scattering effect on thermal conductivity of thin films. *Journal of Applied Physics*, 110:046102, 2011.
- [13] Masahiro Nomura et al. Thermal phonon engineering by tailored nanostructures. *Japanese Journal of Applied Physics*, 57:080101, 2018.
- [14] Bansi Dhar Malhotra Md. Azahar Ali. Nanomaterials in Biosensors: Fundamentals and Applications. *William Andrew*, 2018.
- [15] S.R. Ovshinsky. An introduction to ovonic research. *Journal of Non-Crystalline Solids*, 2:99–106, 1970.
- [16] Manuel Le Gallo and Abu Sebastian. An overview of phase-change memory device physics. *Journal of Physics D: Applied Physics*, 53:213002, 2020.
- [17] G. C. Sosso J. Behler S. Gabardi, S. Caravati and M. Bernasconi. Microscopic origin of resistance drift in the amorphous state of the phase-change compound GeTe. *Physical Review B*, 92:054201, 2015.
- [18] Dambi Park Min Ahn Jeonghwa Han Wonjun Yang Hong-Sik Jeong Mann-Ho Cho Kwangsik Jeong, Seungjong Park. Evolution of crystal structures in GeTe during phase transition. *Nature*, 7:955, 2017.
- [19] A von Hoegen Stefan Maier Ming Xu Ludovica Guarneri, Stefan Jakobs. Metavalent Bonding in Crystalline Solids: How Does It Collapse?. *Advanced Materials*, 33(39):2102356, 2021.

- [20] X. Gonze C. Bichare J. Y. Raty M. Wuttig, V. L. Deringer. Incipient Metals: Functional Materials with a Unique Bonding Mechanism. *Advanced Materials*, 30(51):1803777, 2018.
- [21] Jay Ghatak Suresh Perumal Manisha Samanta, Subhajit Roychowdhury and Kanishka Biswas. Ultrahigh Average Thermoelectric Figure of Merit, Low Lattice Thermal Conductivity and Enhanced Microhardness in Nanostructured $(GeTe)_x(AgSbSe_2)_{100-x}$. *Chemistry - A European Journal*, 23(31):7438–7443, 2017.
- [22] Zhi-Cheng Liu and Lei Wang. Applications of Phase Change Materials in Electrical Regime From Conventional Storage Memory to Novel Neuromorphic Computing. *IEEE Access*, 8:76471 – 76499, 2020.
- [23] SangBum Kim Jiale Liang John P. Reifenberg-Bipin Rajendran Mehdi Asheghi H.-S. Philip Wong, Simone Raoux and Kenneth E. Goodson. Phase change memory. *IEEE*, 98(12):2201–2227, 2010.
- [24] Heinz Disalvo van Dover Gregoire, Lobovsky. Resputtering phenomena and determination of composition in codeposited films. *Physical Review B*, 76(19):195437, 2007.
- [25] R. Gu et al. Nonthermal Transport of Energy Driven by Photoexcited Carriers in Switchable Solid States of GeTe. *Physical Review Applied*, 16:014055, 2021.
- [26] Yaroslav Beltukov Paul Desmarchelier Samy Merabia Ameni Tlili, Valentina Giordano. Enhancement and anticipation of the Ioffe-Regel crossover in amorphous/nanocrystalline composites. *Royal Society of Chemistry*, 11:21502–21512, 2019.
- [27] Valentina Giordano Haoming Luo, Anthony Gravouil and Anne Tanguy. Thermal Transport in a 2D Nanophononic Solid: Role of bi-Phasic Materials Properties on Acoustic Attenuation and Thermal Diffusivity. *Nanomaterials*, 9(10):1471, 2019.

- [28] Nobutomo Nakamura Hirotsugu Ogi and Masahiko Hirao. Picosecond ultrasound spectroscopy for studying elastic modulus of thin films: a review. *Nondestructive Testing and Evaluation*, 26(3-4):267–280, 2011.
- [29] Aurélien Crut Natalia Del Fatti Tatjana Stoll, Paolo Maioli and Fabrice Vallée. Advances in femto-nano-optics: ultrafast nonlinearity of metal nanoparticles. *European Physical Journal B*, 87:260, 2014.
- [30] Vitalyi E. Gusev Pascal Ruello. Physical mechanisms of coherent acoustic phonons generation by ultrafast laser action. *Elsevier*, 56:21–35, 2014.
- [31] Aurélien Crut Jean Lermé, Jérémie Margueritat. Vibrations of Dimers of Mechanically Coupled Nanostructures: Analytical and Numerical Modeling. *The Journal of Physical Chemistry*, 125(15):8339–8348, 2021.